Multiple reflections of solar radiation and photoelectron emission in satellite interaction with space environment

by

Roghaiya Omar

A thesis submitted in partial fulfillment of the requirements for the degree of

Master of Science

Department of Physics

University of Alberta

Abstract

This master's thesis presents a numerical study of the interaction between plasma and spacecraft. The main contribution of my research consists of improving the parameterization of solar illumination and the resulting photoelectron emission from satellite surfaces. The simulations are done with PTetra which is a particle in cell code that uses unstructured tetrahedral meshes to represent spacecraft boundaries and geometries. First, the calculation of photoelectron emission is improved in this work by considering multiple rays of light per surface element instead of a single ray as done in the original version of PTetra. This is done by distributing a number of points per triangular element on each satellite surface. The number of these points is determined from the ratio between the triangle area and the smallest triangle area on any of the structure components. Compared with results obtained with the original version of PTetra, the inclusion of multiple rays per triangle accounts for the possibility of partial illumination of elements due to the fact that part of a given triangle can be exposed to solar radiation, while other parts may be in the shade of physical objects.

The second part of my work considers multiple reflections assuming an arbitrary combination of specular and diffuse reflection. The first step here consists of determining whether a triangular element is exposed to solar radiation. If it is, then secondary rays are traced as per specular or diffuse reflection to determine if they intersect other surface elements. If they do, then the process is repeated until the ray is lost to the outer boundary. The simulations considered use an idealized geometry for the purpose of illustrating the effects of accounting for several rays per surface triangular element and multiple reflections. Then simulations are made with a more realistic geometry corresponding to a component of the Swarm

satellite. In the absence of plasma the effect of multiple reflections is found to be significant. However, with a plasma background representative of the ionosphere, the net effect of multiple reflections on collected current density is negligible.

Acknowledgments

I would like to express my deepest gratitude to my supervisor Prof. Richard Marchand for his full support, encouragement, patience, and understanding in all the time of research and writing of this thesis. Without his guidance and advice, my work would not have been possible.

I would like to thank my thesis committee members, Professors Claire Currie and Ian Mann for their advice and questions during the committee meeting, that helped me see more clearly through this project. I am very grateful to my parents who, despite the distance, with their calls and emails, provided me with unfailing support and encouragement throughout my years of study and research. A very special thank to my husband, and children, for their unlimited love and support. I would not have been able to pursue my study, without their presence in my life.

I would like to thank many friends for their love, care and encouragement, that helped me overcome the difficulties in my graduate study.

Contents

List of Tables

List of Figures

List of Abbreviations

1. **GEO** Geostationary Earth Orbit

2. **IMF** Interplanetary Magnetic Field

3. **LEO** Low Earth Orbit

4. **OML** Orbital Motion Limited Theory

5. **PIC** Particle in Cell

6. **PEO** Polar Earth Orbit

7. **UV** Ultraviolet Radiation

Chapter 1

Introduction

1.1 Space environment

Space outside of Earth atmosphere is not empty as one might think. In addition to the multitude of visible objects such as planets, asteroids and stars, it is permeated with plasma, neutral particles, dust particles and radiation. Near Earth, neutral particles come largely from atoms and molecules leaving our atmosphere. Plasma near-Earth, which consists of free charged particles, comes in part from the ionization of neutral particles escaping the Earth's neutral atmosphere, and from a fraction of the solar wind plasma which penetrates our magnetosphere. Electromagnetic radiation consists of electromagnetic waves coming mainly from the Sun, and it also includes electromagnetic waves reflected by planets and moons, as well as electromagnetic waves originating from other stars or galaxies.

In this thesis, I focus on photoelectron emission caused by solar ultraviolet (UV) radiation, and in particular on the effect of multiple reflections on artificial satellite surfaces. In the following section, I briefly explain some of the main physical aspects and processes of the space environment relevant to man-made satellites.

1.1.1 Solar wind

In the solar system and near-Earth in particular, the Sun is the main source of radiation and plasma governing space weather which in turn affects artificial satellites. The solar wind is a flow of plasma originating from the solar atmosphere. It is made up of electrons and positively charged ions consisting mostly of protons, a small fraction of ionized helium and heavier ions [1]. Solar wind particles take approximately 4 days to reach the Earth's magnetosphere [2]. At Earth orbit under quiet solar activity, the speed of solar wind is approximately 450 km/s, the average temperature is about 10^5K, and its density is approximately 7×10^6 m^{-3} [3]. The solar wind carries a weak magnetic field of approximately 7 nT in the interplanetary space. The interplanetary magnetic field (IMF) is a solar magnetic field which is transported to space by the solar wind. It is known to play an important role in solar wind coupling with planetary magnetospheres. In particular, it plays a role in transferring energy from the solar wind to the magnetosphere [3]. The solar wind parameters however can vary significantly depending on solar activity. For example, the solar wind speed at Earth can be as low as 200 km/s during quiet times or it can be up to 1000 km/s during intense activity.

1.1.2 Magnetosphere

The magnetosphere is a region where the Earth's magnetic field is sufficiently strong to deflect the flow of plasma in the solar wind. The boundary between the magnetosphere and the solar wind shown in Fig. (1.1) is called the magnetopause. The magnetopause extends up to 10 Earth radii in the sun direction. In the downstream region Earth magnetic field is stretched by its interaction with the solar wind to form the magnetotail [4]. The pressure associated with the strong nearly dipolar Earth's magnetic field stops and deflects the incoming solar wind at the bow shock, and it prevents solar wind plasma from directly entering the magnetosphere [5]. The region between the magnetopause and the bow shock is

known as the magnetosheath [5].

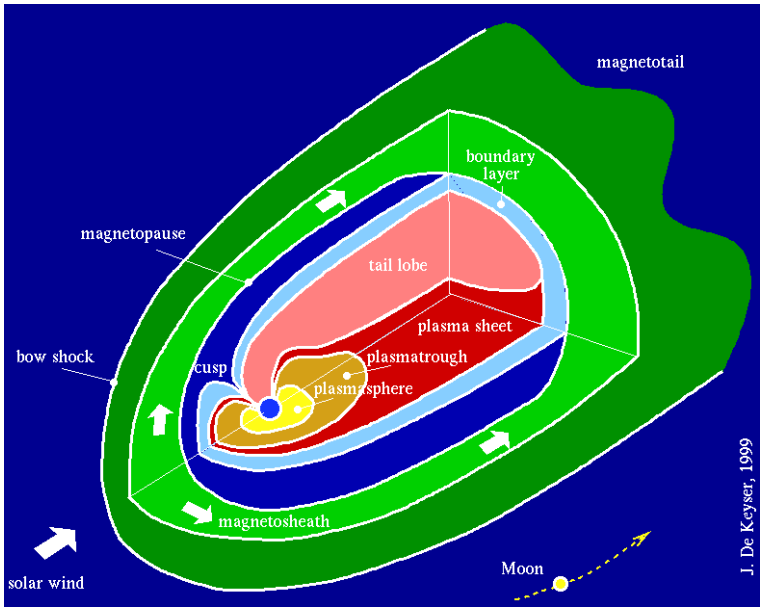

Figure 1.1: Schematic picture of the Earth's magnetosphere.
(http://pwg.gsfc. nasa.gov/istp/outreach/images/Gusts/mag10.gif)

1.1.3 Ionosphere

The ionosphere is a region where atmospheric gases are significantly ionized by solar ultraviolet radiation or by impact with energetic electrons or protons [3]. It is mainly composed of neutral particles and a relatively small fraction of plasma. The ionosphere has a strong influence in forming our near-Earth space environment. It is the main source of charged particles for a high density plasma region referred to as the plasmasphere. It also represents an important source of plasma for the remainder of the magnetosphere, and it is particularly important for communications because it reflects low frequency radio waves. There are three main regions of the ionosphere labeled D, E and F. The lower region D is located at an altitude of approximatively 95 km above Earth surface. It is mainly produced by the ionization of NO (nitric oxide) by solar L-alpha at a wavelength of 1215 $\mathring{A}$, and the ionization of N_2 and O_2 by solar UV at other wavelengths [6]. The E region

is at an altitude ranging from 105 to 110 km above the surface. The ionization in this region is mainly caused by solar X-rays at a wavelength of 1-10 nm and UV radiation at a wavelength of 800-1027 $\mathring{A}$ [6] [7]. At nighttime the E region almost disappears because of weak ionization. The F region is the upper layer of the ionosphere (160, 600) km. It is split into other sublayers F_1 at altitude 150 to 200 km and F_2 above 200 km at day time but these two regions merge into a single region at night time [8]. The electron density in the ionosphere can vary by up to three orders of magnitude depending on the latitude, longitude and local time, as illustrated in Fig. (1.2). The temperature can vary from 10^3K at the lower altitudes, to 10^7K at the higher altitudes extending up to 2000 km. The Earth's magnetic field in these regions is mainly dipolar and a typical value near the equator at an altitude of 400 km is approximately 35 μT. The figure below shows typical day and night profiles of electron density and altitude in the ionosphere. More profiles can be constructed by running the International Reference Ionosphere model (IRI) at a NASA web site: http://omniweb.gsfc.nasa.gov/vitmo/iri2012_vitmo.html

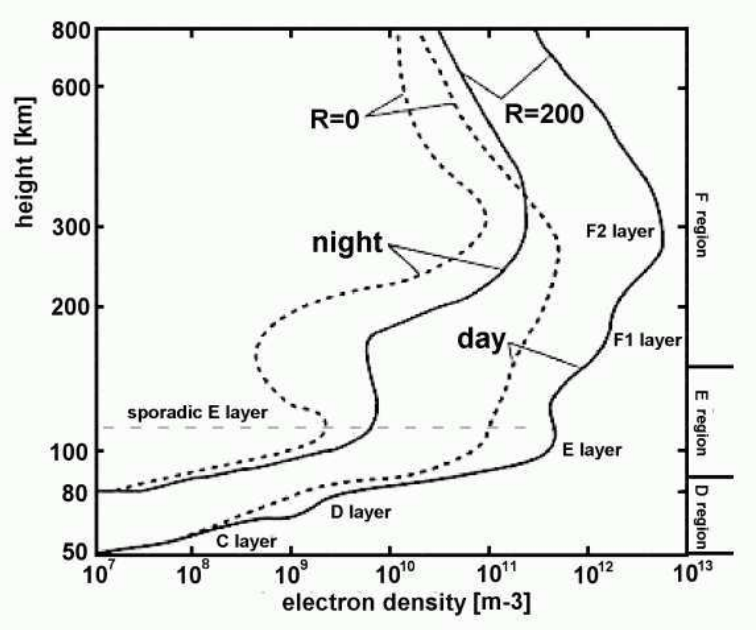

Figure 1.2: Typical day and night profiles of electron density and altitude in the ionosphere.
(http://roma2.rm.ingv.it/en/research_areas/4/ionosphere)

1.1.4 Auroral region

In magnetic polar regions Earth's magnetic field lines are not closed; that is, they don't connect with other magnetic field lines in the opposite hemisphere. In contrast, in lower latitude regions magnetic field lines are closed because they can be traced from one point on Earth to another point called the conjugate point. In polar regions and near the boundary between open and closed magnetic field lines, the ionosphere emits visible light resulting from the excitation and radiative decay of molecules in the upper atmosphere. This phenomenon is know as the aurorae. Auroral radiation is produced at altitudes ranging from approximately 100 to 200 km above Earth's surface.

1.1.5 Radiation belts

The radiation belts were discovered by Van Allen (1958) [9]. They consist of high energy (MeV or above) protons and electrons, that are trapped by the Earth magnetic field. These energetic particles can compromise satellites for example by penetrating internal components and causing electrostatic discharges which can then damage sensitive electronic components [10]. The sources of these energetic particles are the solar wind and the planetary ionosphere [11]. There are generally two belts around the earth. The inner belt which mainly consists of high energy protons, and electrons with energies of hundreds of keV for electrons and tens of MeV for protons. It extends from about 1000 km to 6,000 km in altitude [2]. The outer belt extends between approximately 13,000 to 60,000 km above the surface [2]. It is populated by plasma electrons and ions coming from the solar wind, which are energized as they approach Earth. The exact causes of this energization are still an area of active research, but it is generally believed to to be due to a combination of wave-particle interaction and convection of particles from low to high magnetic field regions [12].

1.2 Plasma

Plasma is ubiquitous in space. A plasma is a gas of charged particles which are not bound to atoms or molecules. A plasma can comprise mainly free electrons and protons as in the solar wind, but it can also consist of negative ions, partly ionized heavy atoms or molecules. The Coulomb potential at a distance r from a point charge q in vacuum is

$$\phi_c = \frac{q}{4\pi\epsilon_0 r}. \tag{1.1}$$

In a plasma, the charge density associated with negatively charged particles is usually nearly canceled by that of positively charged particles. Under this condition, the plasma is said to be "quasi-neutral". Non-neutral plasmas can exist in limited regions of space such as in electric sheaths typically surrounding material objects with which it is in contact.

In a plasma the potential caused by a charged particle, tends to be neutralized by charges of opposite sign, located in a region within a Debye length; that is, within a length

$$\lambda_D = \left(\sum_{i=1}^{N} \frac{n_i q_i^2}{\epsilon_0 k T_i} \right)^{-1/2} \tag{1.2}$$

where n_i is the number of particles of species i per unit volume, q_i and T_i are respectively the charge and temperature of species i, k is Boltzmann's constant and ϵ_0 is the permittivity of free space. As a result, the Debye shielded potential ϕ_D surrounding a point charge q in a plasma in thermodynamic equilibrium is given approximately by

$$\phi_D = \frac{q}{4\pi\epsilon_0 r} e^{\left(-\frac{r}{\lambda_D}\right)}. \tag{1.3}$$

According to most textbooks [5, 13] a classical plasma must satisfy three conditions:

- It must be contained in a medium with scale length much larger than the Debye length

$$\lambda_D << l. \tag{1.4}$$

- The number of particles in a Debye sphere, the so-called "plasma parameter", must be much larger than one.

$$N_D = n_e \lambda_D^3 >> 1. \tag{1.5}$$

- The collision time of charged particles between one another or with a possible neutral background must be much larger than the reciprocal of the plasma frequency. $\omega_p \tau >> 1$.

$$\omega_p = \left(\sum_{i=1}^{N} \frac{n_i q_i^2}{\epsilon_0 m_i} \right)^{1/2}. \tag{1.6}$$

1.2.1 Collisions

Plasma particles can collide with one another as well as with neutral particles when the plasma is not fully ionized. In plasma with a significant density of neutral particles, such as in the Earth's ionosphere, collisions with neutral atoms can be dominant. Assuming a constant neutral collision cross section for simplicity, the ion collision frequency ν_i is then

$$\nu_i = n_n \sigma_n \langle |\vec{v_i} - \vec{v_n}| \rangle, \tag{1.7}$$

where $\sigma_n \simeq \pi d_0^2 \approx 10^{-19} m^2$ is the cross section of neutral particles, n_n is the neutral particles density, and d_0 is the effective radius of a neutral particles. The term in brackets represents the statistical average of the absolute value of the difference between plasma particles of species i and neutral particles. The average distance between collisions or the mean free path is

$$\lambda_n = \frac{\langle v \rangle}{\nu_n} = (n_n \sigma_n)^{-1}. \tag{1.8}$$

In a fully ionized plasma near equilibrium, charged particles collide primarily

with other charged particles due to Coulomb forces [5]. Detailed expressions for Coulomb collision frequencies can be found in most plasma physics textbooks [5, 13]. For example, for stationary thermal electrons colliding with a background stationary thermal distribution of ions of temperature not exceeding the electron temperature, one finds

$$\nu_{ei} = n_e \sigma_c \langle v_e \rangle \approx \frac{n_e e^4}{16\pi\epsilon_0^2 m_e^2 \langle v_e \rangle^3} \tag{1.9}$$

$$\nu_{ei} \approx \frac{\sqrt{2}\omega_{pe}^4}{64\pi n_e} \left(\frac{kT_e}{m_e} \right)^{\frac{-3}{2}} \tag{1.10}$$

$$\nu_{ei} \approx \frac{\omega_{pe}}{64\pi} \frac{ln\Lambda}{\Lambda}, \tag{1.11}$$

where Λ is the Coulomb logarithm Λ and it is of order 10 to 30, depending on the plasma parameters. The electron mean free path is then expressed as

$$\lambda_e \approx 64\pi\lambda_D \frac{\Lambda}{ln\Lambda}. \tag{1.12}$$

A plasma can be treated as being collisionless whenever the collision mean free path is much larger than the scale length of interest, and the collision time, much larger than the timescales of interest.

1.2.2 Magnetic fields in plasma

Most plasmas in the laboratory or in space are permeated with a magnetic field. This magnetic field can be caused by external sources. For example, for space plasmas it can be generated in the Earth's liquid core. It can also be generated by current in the plasma itself as, for example, in shear or compressional Alfvén wave propagating in a magnetized plasma. Charged particles moving in space are affected by the electromagnetic force given by

$$\vec{F} = q\vec{E} + q(\vec{v} \times \vec{B}). \tag{1.13}$$

In equation (1.13), the first term is the electric force, and the second one is the Lorentz magnetic force. In that equation, $\vec{E}$ and $\vec{B}$ are respectively the electric field and the magnetic flux density, q is the particle charge and $\vec{v}$ its velocity. Assuming a vanishing velocity parallel to $\vec{B}$ and a vanishing electric field $\vec{E}$ for simplicity, it can be seen from equation (1.13) that the force will be perpendicular to the velocity and the magnetic field vectors, and particle trajectories will describe circles in a plane perpendicular to $\vec{B}$. This is referred to as the gyro-motion, or the cyclotron motion. The radius (ρ) of this circular motion is called the cyclotron radius or gyro-radius. An expression for ρ can readily be found by balancing the centripetal and magnetic forces as

$$\frac{m\upsilon_{\perp}^2}{\rho} = q(\upsilon_{\perp}B) \tag{1.14}$$

from which it follows that

$$\rho = \frac{m\upsilon_{\perp}}{qB}. \tag{1.15}$$

The cyclotron frequency Ω can also be derived simply from the equations of motion and shown to be

$$\Omega_p = \frac{qB}{m}. \tag{1.16}$$

More generally, particles with a non-zero velocity along the magnetic field, $\upsilon_{\parallel}$, follow helicoidal trajectories with a helix radius which is also given by equation 1.15. For such particles, the pitch angle α is defined as

$$\alpha = \cos^{-1}\left(\frac{\upsilon_{\parallel}}{\sqrt{\upsilon_{\parallel}^2 + \upsilon_{\perp}^2}}\right). \tag{1.17}$$

In the presence of a constant and uniform electric field $\vec{E}$ and magnetic flux density $\vec{B}$, the equation of motion of a point particle of mass m and charge q is

$$m\frac{d\upsilon}{dt} = q(\vec{E} + \vec{v} \times \vec{B}). \tag{1.18}$$

As a result, in addition to following helical trajectories around $\vec{B}$, particles also drift at the so-called $E \times B$ drift velocity given by

$$\vec{v} = \frac{\vec{E} \times \vec{B}}{B^2}. \tag{1.19}$$

Assuming comparable temperatures, the electron's thermal gyro-radius is smaller compared to that of ions by $\sqrt{m_e/m_i}$. Now we can define the ion and the electron magnetization parameters M, used to parameterize the importance of the magnetic field in the plasma surrounding an object. In a Maxwellian plasma, M_α, the magnetization parameter for species α is the ratio of the gyro-radius to the scale length of system

$$M_\alpha = \frac{\rho_\alpha}{L_b}, \tag{1.20}$$

where $\rho_\alpha = v_{th\ \alpha} m_\alpha / (q_\alpha B)$ with $v_{th\ \alpha}$ being the thermal speed of species α, $v_{th\ \alpha} = \sqrt{2T_\alpha/m_\alpha}$. For practical purposes plasma can be considered as unmagnetized when $M_e >> 1$ and $M_i >> 1$. Whereas, plasma is considered magnetized when $M_e << 1$ and $M_i << 1$.

1.3 Interaction of satellites with space environment

Spacecraft have been used for different purposes, including communication, meteorology, navigation, planetary exploration, and remote observations of forests and natural disasters. With time, various processes associated with space environment can affect and compromise spacecraft and their systems. One important process has to do with surface charging and, under certain circumstances, the penetration of internal components by energetic plasma particles. Surface charging can be caused by the collection of electrons and positive ions from the surrounding plasma. It can also result from photoelectron emission when satellite surfaces are

exposed to solar radiation, or to secondary electron emission when surfaces are exposed to the bombardment of sufficiently energetic particles. The result is that the spacecraft potential, the so-called floating potential, is almost always different from that of the local background plasma. Moreover, different parts of a satellite, e.g., solar panels, the main satellite body or its internal components, can be at different potentials. This in turn can lead to unwanted discharges and arcs which can be detrimental to the spacecraft operation.

One important factor which influences the interaction of a spacecraft with its environment is the speed at which it travels. For example, the speed of a satellite following a circular orbit a distance r from Earth center, can be shown to be [14]

$$v_0 = v_{cir} = \sqrt{GM_{\oplus}/r} \tag{1.21}$$

where G is the constant of gravity, $M_{\oplus}$ is the Earth mass and r is radial distance from the Earth's center. For example at Low Earth Orbit (LEO) ($r \approx 6,600$ km) it found that $v_0 \approx 8$ km/s, and at Geostationary Earth Orbit (GEO) ($r \approx 24,000$ km) $v_0 \approx 3$ km/s. When considering the motion of a satellite in the background plasma, two regimes are of interest: supersonic and subsonic flow. In LEO, the ions consist mostly of O^+, temperatures are low ($\lesssim 0.1$ eV) and satellites are supersonic. At higher altitudes, however, ions consist mostly of lighter H^+, temperatures are higher, and satellites are typically subsonic. It should be noted that while satellites are supersonic at lower altitudes, their speed with respect to the background plasma is generally smaller than the electron thermal speed $v_{th\ e} = \sqrt{2T_e/m_e}$.

The plasma environment can affect spacecraft in all types of orbits such as LEO, GEO, and Polar Earth orbit (PEO). However, plasma is not the only component of the environment in space. In order to understand plasma spacecraft interactions it is important to define some conditions of plasma scales where plasma spacecraft interaction occurs. Near spacecraft surfaces, when the length scale l is smaller

than the Debye length, ambient plasma particles will be strongly affected by the presence of the satellite. At larger distances away from the wake however, electric fields associated with the satellite are weak and plasma particles are essentially unaffected by the presence of a satellite.

Another aspect of importance is collisionality. At satellite altitudes, collisions between electrons and ions with one another, or with neutral particle are rare, and the resulting collisions mean free paths are much longer than the Debye length or the scale length of the satellite. For these reasons, plasma can be treated as being collisionless when simulating plasma-satellite interactions.

1.4 Mechanisms of spacecraft charging

Spacecraft charging results from the accumulation of charges on its internal components as a result of the interaction with the space environment. Here is some basic terminology of spacecraft charging.

1. **Surface charging** is caused by relatively low energy particles depositing at the surface of a satellite. If a surface is conducting, the charge collected will distribute so that the surface will be an equipotential. On dielectric surfaces, however, the potential will depend on the position on the surface. Satellites are typically covered with conducting materials in order to prevent the buildup of large potential differences which could then lead to arcing between surface components.

2. **Differential charging** occurs when the spacecraft is composed of different components electrically insulated from one another. The potential difference between components can range from a few volts to several thousands of volts [14]. The charge is not uniform in this case and differential charging can occur depending on the properties of the surface and the environment.

3. **Deep dielectric charging** is caused by high energy electrons and ions ($E >$ 100 keV) penetrating inside satellites, causing the avalanche of secondary electrons, possibly leading to deep dielectric charging.

1.5 Electrical current source to spacecraft

1.5.1 Plasma current collection

The ambient plasma is an important source of the current collected by a spacecraft. For simplicity a Maxwellian distribution function can be used to estimate the floating potential of spacecraft in plasma. The current density collected per unit surface area is given by the integral over the particle distribution function for a given particle species

$$J = -q \int \int \int \vec{v} \cdot \hat{n} f(v) d^3 v \tag{1.22}$$

where $\vec{v}$ is the velocity of particles, $\hat{n}$ is the normal vector to the surface pointing outward and q is the particle charge . In order for this integration to be evaluated, the distribution function and the limits of the integral must be specified. For current density incident on a surface the velocity integration must be over all velocities pointing toward the surface; that is, all velocities such that $\hat{n} \cdot \vec{v} < 0$.

1.5.2 Backscattered and secondary electrons

When an electron impacts a surface, it can be reflected or absorbed. If absorbed, it may collide with some other atoms and reverse direction and backscatter out of the material. The probability of generating a scattered electron depends on material properties, primary electron energy and the primary electron incidence angle. On the other hand, this absorbed electron can transfer energy to one or several other electrons which could then escape from the material. This is called secondary electron emission. Electrons with energies below a certain threshold cannot lead to electron emission, and only sufficiently energetic electrons can cause such emission.

The secondary electron yield δ_e as a function of energy E and incidence angle θ can be approximated by

$$\delta_e(E,\theta) = \frac{1.14\delta_{max}}{\cos\theta}\left(\frac{E_{max}}{E}\right)^{0.35}\left(1 - exp\left(-2.28\cos\theta\left(\frac{E_{max}}{E}\right)^{1.35}\right)\right) \quad (1.23)$$

where E_{max} is the energy at which the yield is maximum and equal to the yield δ_{max} at normal incidence [14].

Table (1.1) (from Katz et al.1977) [14] gives some representative values of the maximum yield δ_{max} and E_{max} [14].

Backscattering differs from secondary emission by the energy of the emitted electrons. Secondary electrons are mainly emitted with energies of only a few eV. Backscattered electron however, may have an energy close to that of the primary electron. Backscattering is generally caused by incident electrons with energy larger than 50 eV [15].

Ions at high energy can also penetrate surfaces or scatter causing secondary electron emission. A small fraction of ions can be re-emitted but they are generally neglected in surface potential calculations [15]. In some cases the flux of secondary electrons emitted at a surface caused by electron or ion impact can be more than the incident flux, which leads to a positive charge on the spacecraft surface [14].

Table 1.1: Representative values for maximum yield δ_{max} and E_{max} of secondary electrons resulting from electron impact (from Katz et al., 1977).

Material	δ_{max}	E_{max} (keV)
Aluminum	0.97	0.3
Aluminum oxide	1.5-1.9	0.35-1.3
magnesium oxide	4.0	0.4
silicon dioxide	2.4	0.4
Teflon	3	0.3
Kapton	2.1	0.15
magnesium	0.92	0.25

1.5.3 Photoelectron emission

In addition to back-scattered and secondary electron emission, photoelectron emission can also contribute to the current balance in a spacecraft. Many materials emit electrons when they are exposed to solar radiation in the UV range $< 2000\mathring{A}$ [15]. Photoelectron current depends on the solar flux, the material properties, the spacecraft potential, and the angle of incident of solar radiation. Rumsh et al. (1960) [15] have shown that the emitted photoelectron current depends on the wavelength. Samson and Cairns (1965) [15] also found that for aluminium, as the wavelength changes from 300 to 1300 $\mathring{A}$, the angular dependence of the yield decreased [15]. For example table (1.2) shows two results of current densities at normal incidence for different materials obtained by Feuerbacher and Fitton (1972) [15] and Hastings (1996) [14].

Table 1.2: Photoelectron emission characteristics and current densities at normal incidence

Material	Work function	$\lvert j_{ph_0} \rvert$ $(\frac{\mu A}{m^2})$ (Feuerbacher and Fitton 1972)	$\lvert j_{ph_0} \rvert$ $(\frac{\mu A}{m^2})$ (Hastings 1996)
Aluminium	3.9	48	42
Gold	4.8	29	29
Stainless steel	4.4	24	20
Vitreous carbon	4.8	21	13
Graphite	4.7	7.2	4
Indium oxide	4.8	32	30

1.5.4 Effect of magnetic and electric fields on current collection

Spacecraft are affected by the ambient magnetic field. In the rest frame of a satellite there is a so-called motional or convection electric field associated with plasma flow velocity with a component perpendicular magnetic field. This electric field is given by

$$\vec{E} = -\vec{v} \times \vec{B}. \tag{1.24}$$

It is the electric field which corresponds to the drift velocity $\vec{E} \times \vec{B}/B^2$ in the satellite frame of reference. This convection electric field corresponds to a potential gradient in the background plasma. This in turn leads to differences between the satellite potential and nearby plasma potential depending on the position on the satellite surface.

A magnetic field can also cause anisotropy in collected particle fluxes due to the fact that charged particles gyrate around magnetic fields [14, 16]. If the speed of these particles in the direction parallel to $\vec{B}$ is larger than the $\vec{E} \times \vec{B}$ drift speed, then particles are effectively confined to flux tubes of a few thermal gyro-radii in diameter, and the source of electrons incident on satellite surfaces are effectively

limited to these magnetic flux tubes.

1.6 Spacecraft-environment interaction models

Different models have been developed to analyze spacecraft-environment interaction. Some have been sponsored by government agencies, while others have resulted from individual initiatives carried out in universities. The following gives a brief description of the main models currently in use. NASCAP_2k is developed under contract for NASA (National Aeronautics and Space Administration) and the US Air Force[17]. It is a 3D model designed to calculate the interaction between spacecraft and different plasma backgrounds, such as geosynchronous, interplanetary, auroral, and LEO plasma environments. It can be used to simulate surface charging, floating potentials and volume charging under a broad variety of conditions [18]. MUSCAT (Multi Utility Spacecraft Charging Analysis Tool) has been developed since 2004 [19] by Professor Cho's team at Kyushu Institute of Technology [17]. MUSCAT is a three dimensional code, and it uses an structured Cartesian mesh. It is applicable to a wide range of space plasma conditions including LEO, PEO and GEO. It comes with a full Graphical User Interface designed for engineers who may not be familiar with computer simulation techniques or detailed processes of spacecraft plasma interaction.

SPIS (the Spacecraft Plasma Interaction System) is an open source code. It was developed under contract for the European Space Agency (ESA), and it is available freely to anyone in the world [20]. It is a 3D electrostatic particle in cell code written in Java [17, 21]. It uses an unstructured tetrahedral mesh, and it works based on a numerical simulation called SPIS NUM [21]. SPIS accounts for surface interaction including photoelectric emission and secondary electron emission from both electron and ion impact.

EMSES (The Electromagnetic Spacecraft Environment Simulator) is a 3D electromagnetic particle in cell simulation model (Miyake and Usui, 2009) [22]. It uses

a structured Cartesian mesh. It is parallelized and can run on thousands of processors. EMSES can be used to study the interaction between spacecraft and plasma including the variations of spacecraft potential under a variety of space environment conditions [23].

iPic3D (implicit Particle-in-Cell code) is a 3D electromagnetic PIC code, written in C++ [17]. It is used for plasma multi-scale simulation by solving Vlasov-Maxwell system [24]. It also uses a structured Cartesian mesh. It is based on the implicit moment method, and it is parallelized and can run on thousands of processors.[24].

PTetra is a simulation code which calculates the interaction between a spacecraft and the surrounding environment. It treats all particle species kinetically, using the particle in cell method [17], and it uses an unstructured tetrahedral mesh. It is capable of representing realistic satellite geometries and it is well-suited to imposed physical boundary conditions on satellite components. PTetra is an electrostatic time-dependent code however, and it can account for a constant and uniform magnetic field and it can be used to calculate first order magnetic field perturbations [17].

The six models mentioned above may differ in the numerical approaches that they use, but they all account for the same important physical processes of satellite interaction with space environment, such as surface charging, photoelectron emission, secondary electron emission and the effect of an ambient magnetic field.

1.7 Objectives

The objective of this thesis is to develop and implement an algorithm in the satellite-environment simulation model PTetra, to improve the calculation of photoelectron emission resulting from solar UV radiation. This is done by a) replacing the original stepping strategy to follow light rays with a more efficient ray tracing approach, b) accounting for multiple rays per triangular surface element instead

of only one in the original version of the code, and c) accounting for multiple reflections of solar radiation.

Chapter 2

Spacecraft as a Langmuir probe

The physics of spacecraft charging is similar to that of the interaction of a Langmuir probe in a plasma. The first analysis of electrostatic probes used to infer plasma properties was presented by Langmuir and Smith in 1926 [25]. In the following I summarize the simplest form of this model referred to as the Orbit (or Orbital) Motion Limited (OML) theory, which is still frequently used to interpret Langmuir probe measurements. A Langmuir probe is a small spherical or cylindrical electrode which, when immersed in a plasma, can be used to determine some of its properties. The principle is simple: The probe is biased electrically with respect to a ground and its characteristic, that is, the current that it collects as a function of the bias voltage, can be used to infer the plasma density and temperature.

A satellite in space is similar to a probe in a plasma, with one important difference: It usually collects nearly zero net current. Indeed, except for satellites equipped with ion thrusters or electron guns, the potential of a spacecraft with respect to space environment cannot be controlled actively. The so-called "floating potential" of a spacecraft is determined from several processes of satellite-environment interaction, such as collection of charged particles from the surrounding plasma, or the emission of photoelectrons or secondary electrons. In the simplest case, for example, where only collection of plasma particles are at play, a satellite is typically negatively charged and its floating potential is negative. This

is due to the fact that electrons typically have a much larger thermal speed than the heavier ions. As a result, if a satellite is initially not charged, electrons will precipitate on its surface in larger numbers than ions. The satellite will then charge negatively until its negative potential is sufficient to repel just enough electrons so that the current associated with the electron flux is balanced by that of the ion flux. When ions impact the satellite, most of them will combine with electrons at the surface producing neutral atoms [25]. These neutrals are not considered in the probe current collection. Conversely in situations where photoelectron or secondary electron emission would dominate, the spacecraft would charge positively until its potential is sufficiently high to retain otherwise escaping electrons so as to have a zero net collected current. The floating potential of a satellite V_{float} is the potential at which the satellite collects no net current. The different contributions to the current collected by a satellite are a function of the potential V_s with respect to its environment. These contributions include:

I_e = Net incident current from electron plasma background.

I_i = Net incident current from ion plasma background.

I_{se} = Net current from emitted secondary electrons associated with electron impact.

I_{si} = Net current from emitted secondary electrons associated with ion impact.

I_{ph} = Net current associated with photoelectron emission.

I_b = Active current sources, as from thrusters or electron guns.

The net current of the satellite plasma is the sum of all these currents [14].

$$I_{net} = I_e(V_s) + I_i(V_s) + I_{se}(V_s) + I_{si}(V_s) + I_{ph}(V_s) + I_b(V_s). \tag{2.1}$$

As mentioned previously, under most conditions, satellites are in current balance; that is, $I_{net} = 0$.

2.1 Orbital motion limited (OML) theory

The OML theory was first introduced by Mott-Smith and Langmuir [26] as a means to interpret the characteristics of probes in a laboratory plasma. While limited in scope and not directly applicable to satellites, it does capture important aspects of satellite interaction with space environment, which is why it is useful to briefly review it here.

The OML theory applies to small electrical probes in low density collisionless plasmas [27, 26]. Since the seminal work of Mott-Smith and Langmuir, many studies have been made to understand the response of biased probes in plasmas under more realistic conditions including, for example, collisional or magnetized plasmas [28, 29], high density plasmas [30], non-thermal plasmas [31], and flowing plasmas. A first computational analysis of spherical and cylindrical characteristics has been made by Laframboise [25], and more recently several authors have developed mathematical and computational models to better describe and understand probe characteristics under more realistic conditions [15, 32, 31].

It should also be noted that several articles have been published over the years, in which limitations of the OML theory has been described, and improvements proposed [27, 33]. In the following, the simplest form of the OML theory is presented in order to explain the basic process of current collection by a charged body in a plasma.

The Orbital Motion Limited theory (OML) is valid under certain assumptions such as: the system is at a steady state, collisions between electrons and ions are negligible, and all particles come from infinity where the electric potential is zero. The OML theory is strictly valid only if the Debye length is much larger than the impact parameter of collected particles. Referring to Fig.(2.1), the impact parameter is the closest distance that the incident particle would come to the center of the sphere if it were not deflected.

2.2 Current Collection by a Spherical Probe

Let us consider particles collected by a spherical probe of radius R and potential V with respect to the background plasma.

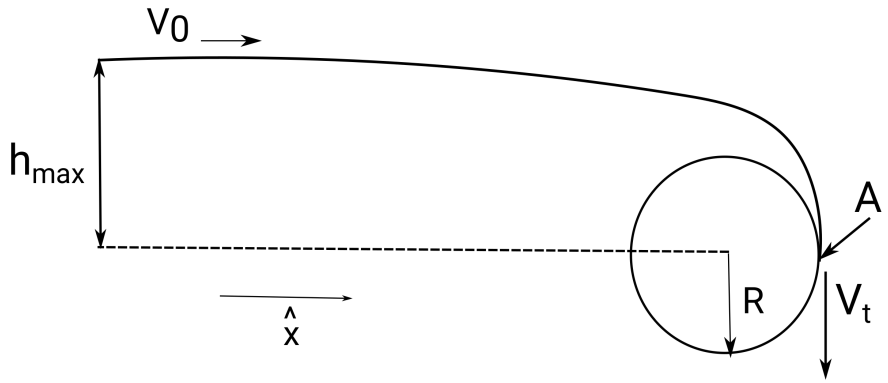

Figure 2.1: Illustration of an attracted particle trajectory as it approaches a spherical probe.

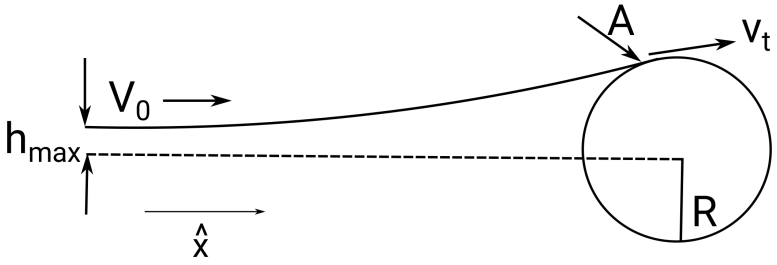

Figure 2.2: Illustration of the maximum impact parameter of a repelled particle.

Plasma is assumed to be Maxwellian and for simplicity the probe is assumed to be much smaller than the plasma Debye length so that the forces affecting particles approaching the probe are well-approximated by unshielded Coulomb forces. Referring to Fig. (2.1) let us consider particles coming toward the probe with a velocity $\vec{v} = v_0\hat{x}$ far from the probe, and impact parameter h. It can be

seen that the largest impact parameter h_{max} for which particles will be collected (i.e., impact the the sphere), is such that the particle trajectory will intersect the sphere surface tangentially at point A. A relation between h_{max} and v_0 can be derived straightforwardly from conservation of energy and angular momentum as follows. Assuming zero potential far from the probe, energy conservation gives

$$\frac{1}{2}mv_0^2 = \frac{1}{2}mv_t^2 + qV, \tag{2.2}$$

where v_0 and v_t are respectively the incident speed at infinity and the tangential speed at impact. Similarly, conservation of angular momentum gives

$$mv_0 h_{max} = mv_t a, \tag{2.3}$$

where a is the sphere radius. Solving for h_{max} then yields

$$h_{max} = a^2 \left(1 - 2q\frac{V}{mv_0^2}\right)^{\frac{1}{2}}. \tag{2.4}$$

The sphere can be attractive or repulsive. If the potential of the sphere is negative, ions will be attracted and electrons will be repelled. Conversely, electrons will be attracted and the ions repelled if the potential is positive. To be specific let us now assume a Maxwell- Boltzmann distribution function for incident particles

$$f(v) = n\left(\frac{m}{2\pi kT}\right)^{\frac{3}{2}} e^{\frac{-mv^2}{2kT}}, \tag{2.5}$$

when the potential of the sphere is attractive, the flux Γ of collected particles is given by

$$\begin{aligned} \Gamma &= \int_0^\infty v^3 f(v) 4\pi a^2 \left(1 - \frac{2qV}{mv^2}\right) dv \\ &= a^2 n \left(\frac{8kT\pi}{m}\right)^{\frac{1}{2}} \left(1 - \frac{qV}{kT}\right). \end{aligned} \tag{2.6}$$

Similarly for a repulsive sphere the flux of collected particles is given by

$$\begin{aligned}\Gamma &= \int_{v_1}^{\infty} v^3 f(v) 4\pi a^2 \left(1 - \frac{2qV}{mv^2}\right) dv \\ &= a^2 n \left(\frac{8kT\pi}{m}\right)^{\frac{1}{2}} e^{\frac{-qV}{kT}}, \end{aligned} \tag{2.7}$$

where the minimum speed is defined by

$$v_1 = \sqrt{\frac{2qV}{m}} \tag{2.8}$$

where n is the density of plasma, m and q are respectively the mass and charge of a plasma particle, T is the temperature and Γ is the flux of particles. The current on the probe is the sum of the electron and ion currents. In equations (2.6) and (2.7) putting $I = q\Gamma$ we obtain an expression for the current from attracted and repelled particles. For attracted particles, assuming a unit charge for simplicity:

$$I = qa^2 n \left(\frac{8kT\pi}{m}\right)^{\frac{1}{2}} \left(1 - \frac{qV}{kT}\right), \tag{2.9}$$

and for repelled particles:

$$I = qa^2 n \left(\frac{8kT\pi}{m}\right)^{\frac{1}{2}} e^{\frac{-qV}{kT}}. \tag{2.10}$$

Assuming a negative probe potential ($V < 0$), electrons will be repelled and ions attracted, the total current will be

$$I_{total} = -ea^2 n_e \left(\frac{8\pi kT_e}{m_e}\right)^{\frac{1}{2}} e^{\frac{eV}{kT_e}} + Zea^2 n_i \left(\frac{8\pi kT_i}{m_i}\right)^{\frac{1}{2}} (1 - \frac{ZeV}{kT_i}), \tag{2.11}$$

where Z is the average ion charge. It is convenient to define the total normalized current $\tilde{I}$ as

$$\tilde{I} = I_{total} \frac{1}{n_e a^2 e} \left(\frac{m_e}{8\pi kT_e}\right). \tag{2.12}$$

From the equations above, it follows that

$$\tilde{I} = -e^{\frac{eV}{kT_e}} + Z\left(\frac{m_e}{m_i}\right)^{\frac{1}{2}}\left(\frac{T_i}{T_e}\right)^{\frac{1}{2}}\left(1 - \frac{zeV}{kT_i}\right). \tag{2.13}$$

Conversely for a positive potential ($V > 0$), the ions will be repelled and the electrons attracted, so that the total current is

$$I_{total} = -ea^2 n_e\left(\frac{8\pi kT_e}{m_e}\right)^{\frac{1}{2}}\left(1 - \frac{eV}{kT_e}\right) + Zea^2 n_i\left(\frac{8\pi kT_i}{m_i}\right)^{\frac{1}{2}} e^{\frac{-ZeV}{kT_i}}. \tag{2.14}$$

Using equation (2.12) to get the normalized current for the positive probe potential ($V > 0$) we find

$$\tilde{I} = -\left(1 + \frac{eV}{kT_i}\right) + Z\left(\frac{m_e}{m_i}\right)^{\frac{1}{2}}\left(\frac{T_i}{T_e}\right)^{\frac{1}{2}} e^{\frac{zeV}{kT_i}}. \tag{2.15}$$

Figure (2.3) shows the relation between the current and the floating potential. Dots correspond to calculations made by Laframboise in his thesis [25]. In this comparison, it is assumed that $T_e = T_i$.

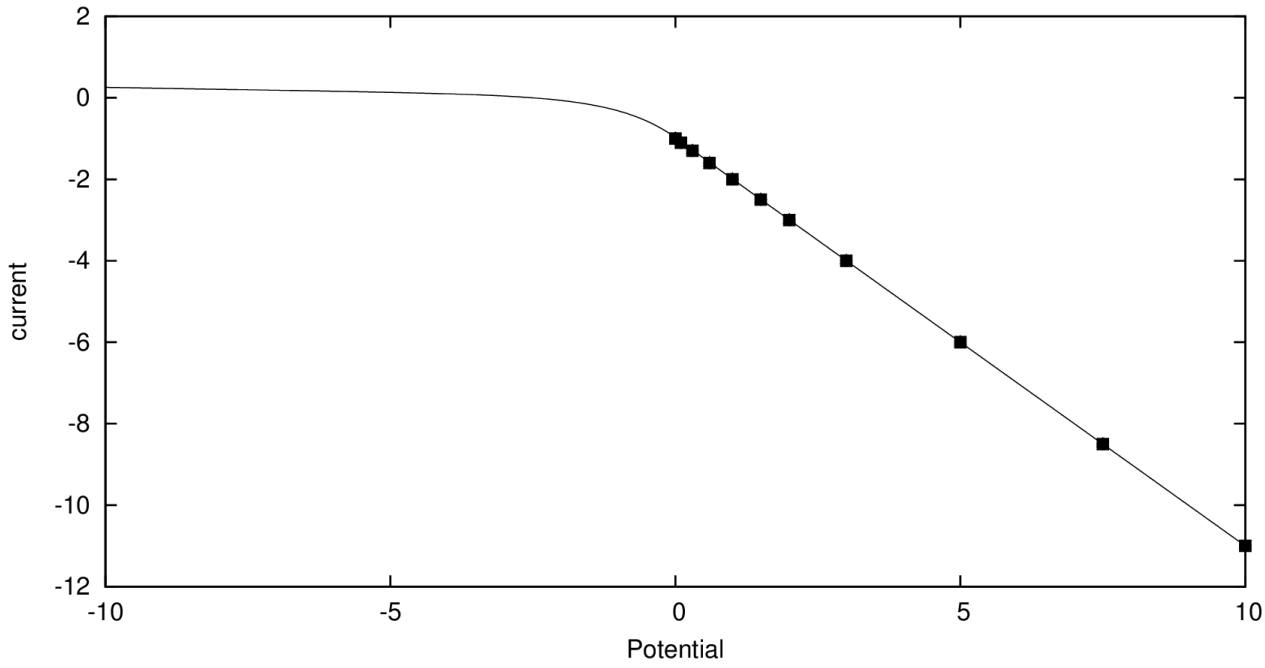

Figure 2.3: Comparison between the normalized characteristic calculated for a spherical probe with Eqs. 2.13 and 2.15 and from tabulated values in Laframboise's thesis (dots).

Chapter 3

Numerical approach

3.1 Mesh definition and generation

In order to describe numerically physical processes occurring in space it is usually necessary to use a mesh, or a grid. Computational meshes are made of points or vertices, which are connected in order to define cells or elements. It is customary to distinguish between two broad families of meshes: structured and unstructured. Examples of structured meshes induce uniform Cartesian grids and grids based on polar or cylindrical coordinates. Unstructured meshes can be constructed, for example, with triangular elements in two dimensions, or tetrahedra in three dimensions. The general distinction between structured and unstructured meshes is that in the former, there is a simple and implicit relation between a cell or vertex and its neighbours. For example, in a uniform 2D Cartesian grid, each vertex can be labeled with two indices i and j and the neighbours of such a vertex are labeled $i \pm 1$, j and i, $j \pm 1$. With unstructured meshes, however, no such relations exist and it is necessary to list all vertex coordinates, their connectivity, and cell neighbors (or adjacency) in a data structure. As an example, a simple triangular mesh consisting of only four triangles, is shown in Fig. (3.1).

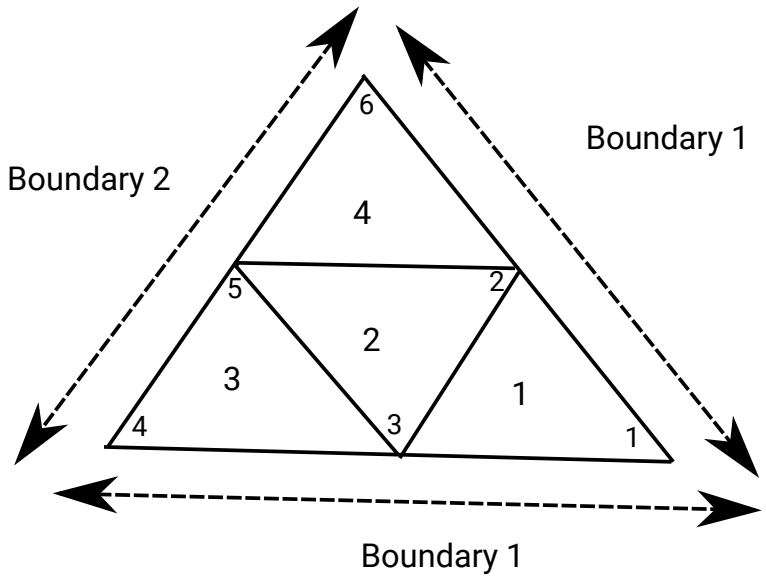

Figure 3.1: A Simple Representation of 2D triangular mesh.

Table 3.1: Data structure of the triangular mesh shown in Fig. 3.1.

Elements	Vertices	Adjacency
1	3, 1, 2	-1, 2, -1
2	3, 2, 5	4, 3, 1
3	4, 3, 5	2, -2, -1
4	5, 2, 6	-1, -2, 2

Table (3.1) shows how the information describing the simple mesh illustrated in Fig. (3.1) is listed in a file. In addition to the x and y coordinates for each vertex (not shown in the table), each element is defined by its own index (first column) followed by the indices of its three vertices (columns 2-4), followed by the indices of the three adjacent triangles opposite each vertex (columns 5-7). In this example, element 2 is made of vertices 3, 2, and 5. The element opposite the first listed vertex (3) is element 4, the element opposite the second listed vertex (2) is the element with index 3, and so on. Note that some indices in the adjacency list are negative, for example the first and the second adjacency of the element 1.

This refers to physical boundaries in the simulation domain. It is used in the PIC code and by the Poisson solver to identify boundaries on which different boundary conditions can be imposed. Finally we note that when listing vertex indices making a triangular element, the convention is to list them anti-clockwise. This convention is useful when determining whether a point is in a given element or not. It is also useful for finding the index of a triangle containing an arbitrary point. Essentially the same procedure is used to represent a tetrahedral mesh in 3D. As illustrated in Tables 3.2 and 3.3, the mesh is defined with a list of x, y, z coordinates for each vertex. Then follows a list of tetrahedra indices, connected vertices and adjacent elements. As with a triangular mesh, these are indices of tetrahedra opposite the four vertices. Here also negative indices are used to identify boundary indices.

3.2 Idealized geometry

We now introduce an idealized geometry constructed for the purpose of illustrating multiple reflections in PTetra. It consists of two blocks of height and width 2.8 cm, and thickness 0.4 cm. The blocks are separated by 2 cm. A cylinder with height 1.8 cm and radius of 0.4 cm is centered between these two blocks, on which multiple reflections can take place. The simulation domain is delimited by a cubic boundary with sides of height of 3.6 cm as shown in Fig. (3.2). The gmsh file defining the complete geometry used to construct the mesh is given in the Appendix. Table (3.2) shows the coordinates of the vertices of the first four elements. Table (3.3) shows the indices of the first four tetrahedra, the indices of their vertices, and the indices of the element opposite each vertex. In this geometry the mesh resolution was chosen so as to give a good representation of the three objects considered. Since no plasma is considered here, the mesh resolution is otherwise unimportant.

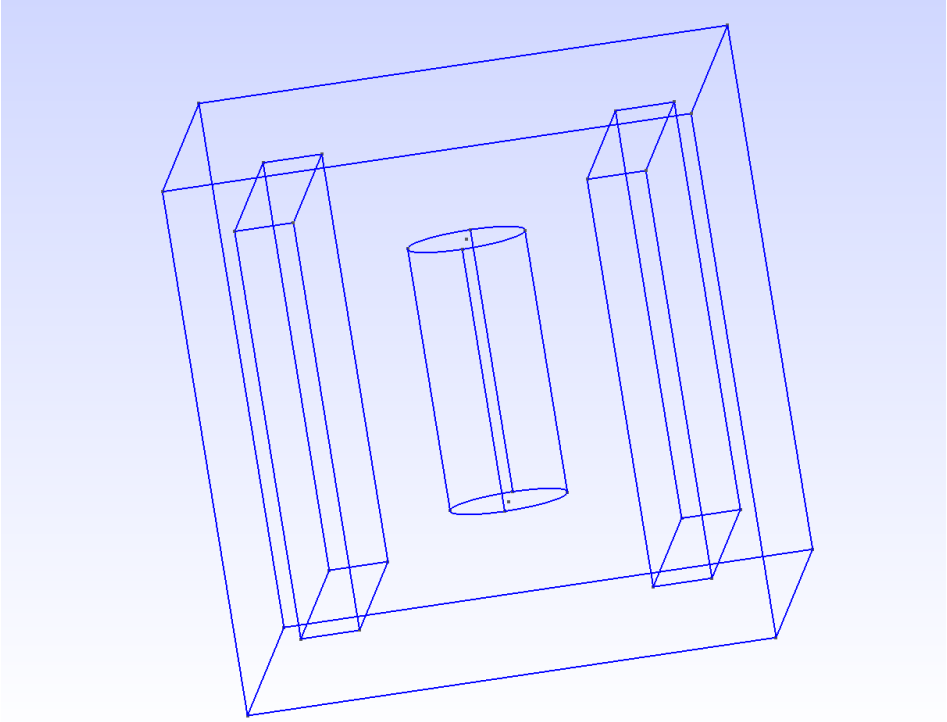

Figure 3.2: Illustration of the test geometry used to demonstrate the effects of multiple reflections. The two rectangular prisms have dimensions of $2.8 \times 2.8 \times 0.4$ cm, and the central cylinder has a height of 1.8 cm and a radius of 0.4 cm.

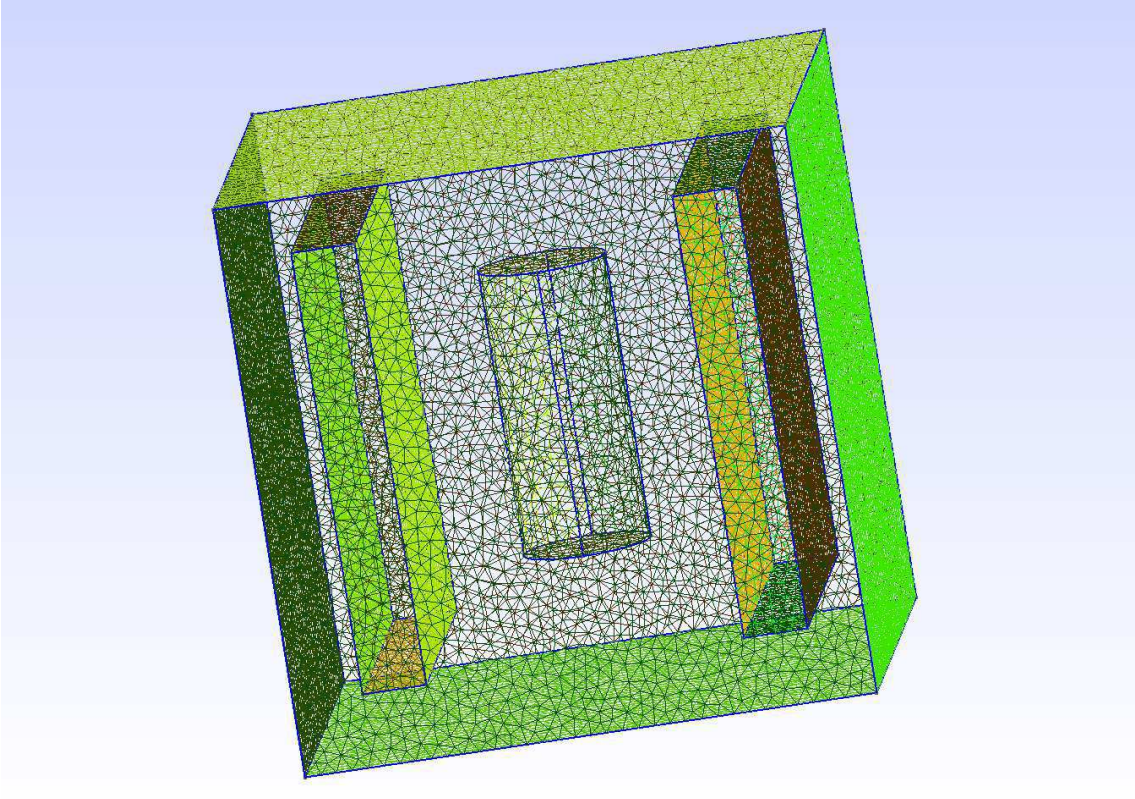

Figure 3.3: Illustration of the 2D surface mesh on the idealized geometry .

Table 3.2: Coordinates of vertices of element 1.

Vertices	Coordinates
1	-1.8000000000000000E+00, -1.8000000000000000E+00, -1.8000000000000000E+00
2	1.8000000000000000E+00, -1.8000000000000000E+00, -1.8000000000000000E+00
3	-1.8000000000000000E+00, 1.8000000000000000E+00, -1.8000000000000000E+00
4	1.8000000000000000E+00, 1.8000000000000000E+00, -1.8000000000000000E+00

Table 3.3: Data structure of a 3D mesh.

Elements	Vertices	Adjacency
1	19025, 17594, 23364, 25599	84136, 1755, 9909, 13284
2	8292, 17310, 20184, 22685	11441, 28808, 2557, 13271
3	18159 20895 16514 24627	1049 58440 11048 338
4	16490 19840 17643 23636	3177 7866 1760 8730

The four neighbors of a tetrahedron are associated with the vertices to which they are opposite. For example element 1 is made of vertices 19025 17594 23364 25599 and its four neigbours are 84136 1755 9909 13284. The face opposite to the first vertex (with index 19025); that is, the face made of vertices with indices 17594, 23364 and 25599 is adjacent to a element 84136. Similarly, the face opposite the second vertex (index 17594), its adjacent is element 1755.

3.2.1 Connectivity of points

At this point is interesting to mention something about the way vertices are connected when constructing an unstructured triangular (2D) or tetrahedral (3D) mesh. Given a distribution of points in space, there are generally very many ways to connect them into triangles or tetrahedra. One method which produces simplexes (triangles in 2D and tetrahedra in 3D) that are as "compact" or equilateral as possible is based on the Delaunay criterion [34, 35, 36]. This criterion works as follows in two dimensions. If no point in the mesh is inside the circumscribing circle of every triangular element, then the resulting mesh is said to be "Delaunay". The criterion is the same in three dimensions: If no mesh point is in inside the circumscribing sphere of every tetrahedron in the mesh, then the mesh is also said to be "Delaunay". Given a triangular or tetrahedral mesh, it is then possible to define a so-called "dual mesh" by constructing "Voronoi cells" around every mesh vertex. This is done by constructing perpendicular bisectors (lines in 2D and planes in

3D) on every element edge. The domain containing mesh vertices and delimited by the closest bisectors is the Voronoi cell at that vertex [37]. Given a distribution of vertices in space, the Voronoi cell surrounding a point can equivalently be constructed as the volume delimited by the closest perpendicular bisectors defined on segments joining this point and every other mesh vertices.

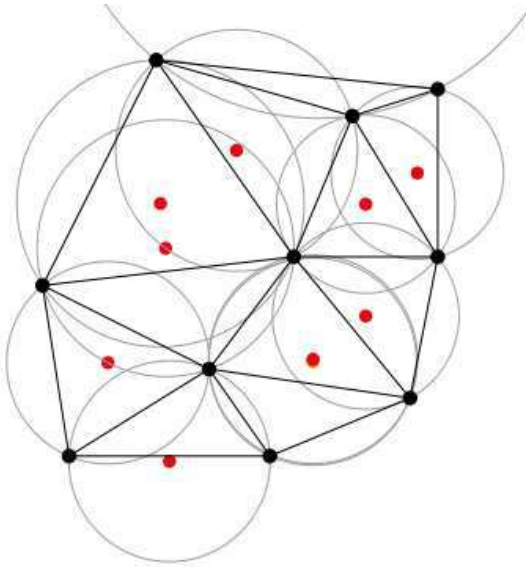

Figure 3.4: Illustration of a Delaunay triangulation with all the circumcircles and their centers (in red).
(https://en.wikipedia.org/wiki/ Delaunay_triangulation)

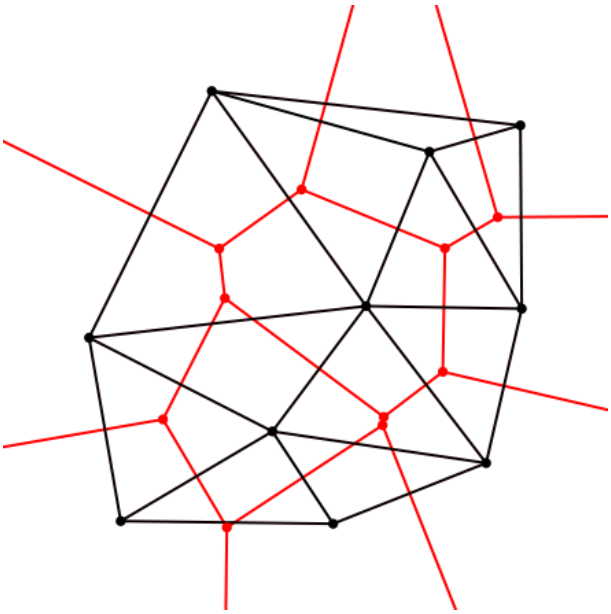

Figure 3.5: Voronoi cells can also be constructed by connecting the centre of every circumscribing triangle (in red) with all others with which it shares the side of a triangle. (https://en.wikipedia.org/wiki/Delaunay_triangulation)

3.3 Solar illumination

3.3.1 Stepping strategy

In the original version of PTetra, the method used to determine whether a triangle is illuminated by the Sun or not was based on a stepping strategy. In this approach a point located at the center of each triangle on a satellite surface element is used as an initial position from which small steps are made in the direction of the Sun. The step size was defined as a small fraction of the linear scale of the smallest mesh element. Specifically, the step size was defined as $\delta = 0.1(V_{min})^{1/3}$, where V_{min} is the smallest tetrahedron volume in the entire mesh. If this stepping process resulted in the path crossing a physical object represented in the mesh, the triangle was treated as being entirely in the shade of that other object. If, on the other hand, the stepping process led to the path reaching the outer boundary without crossing any physical object, then the triangle was considered to be fully exposed

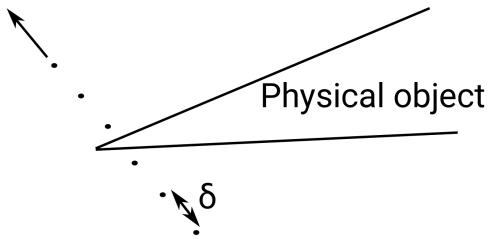

Figure 3.6: Illustration of a step passing through a physical object in the mesh

to solar radiation. One shortcoming of this approach was that triangles (large or small) were considered to be either fully illuminated or completely in the shade. No account was made for the possibility of a triangle to be partly illuminated and partly in the shade. Another possible problem comes from finite step size used. While unlikely, it is always possible that marching paths will step through a sharp edge of a physical object as shown in Fig. (3.6), and result in a triangle being illuminated instead of being in the shade. These shortcomings motivated the improvements described in the following paragraphs.

3.3.2 Ray tracing

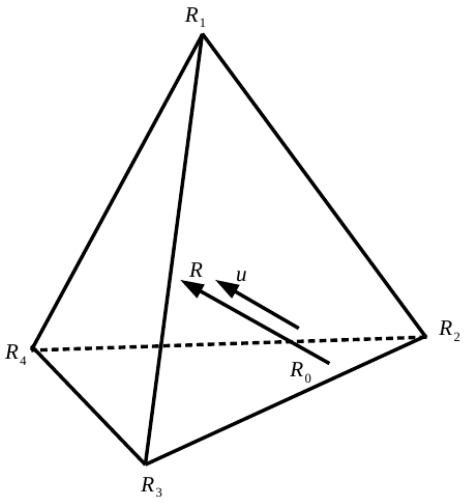

Figure 3.7: Illustration of ray tracing along direction $\vec{u}$ from one point $\vec{R}_0$ in a face of a tetrahedron to another point $\vec{R}$ in one of the three other faces.

Ray tracing is done by considering a point $\vec{R}_0$ in a triangular face, and finding the intersection between the line going through $\vec{R}_0$ and directed along $\vec{u}$ with one of the tetrahedral faces. This process will continue marching from tetrahedron to tetrahedron toward the Sun direction until either crossing a physical object in the mesh or reaching the outer boundary. For computing intersections of lines and a plane, we use the parametric equation representation for a line. A point in a triangle can be defined as:

$$\vec{R} = \vec{R}_1 + S_1(\vec{R}_2 - \vec{R}_1) + S_2(\vec{R}_3 - \vec{R}_1) \tag{3.1}$$

and the parametric equation of the line is:

$$\vec{R} = \vec{R}_0 + t\vec{u} \tag{3.2}$$

where $\vec{R}_1, \vec{R}_2$ and $\vec{R}_3$ are the vertices of a triangular face of a tetrahedron, $\vec{u}$ is a vector that provides the line's direction and $\vec{R}_0$ is a starting point. In order to have the intersection point inside the triangle, the solution to Eqs. (3.1) and (3.2) must satisfy this condition

$$S_1 > 0, S_2 > 0, S_1 + S_2 <= 1. \tag{3.3}$$

When a single point per triangular face is considered and the stepping process encounters a physical object along the path to the Sun, the triangle is treated as being entirely in the shade of that object. On the other hand, when the ray reaches the outer boundary without encountering any physical object, then, the triangle is considered to be fully exposed to solar radiation. From tetrahedron to tetrahedron the intersection point $\vec{R}$ is used as new starting point, and the process is repeated until the the point reaches a physical object or the outer boundary.

3.3.3 Multiple points per triangle

An improvement to the calculation of surface illumination consists of applying the ray tracing technique described above with multiple points distributed in each triangle, instead of only one. Every point is assigned a weight equal to the reciprocal of the number of points in a given triangle. The number of points used in a triangle is determined from the ratio between the triangle area and the smallest triangle area on any of the structure components. Two methods have been considered to distribute these points: a random distribution, and a structured, uniform distribution. Both types of distributions were found to produce similar results and a uniform distribution of points has been adopted in the calculations which follow.

3.4 Multiple reflections

Reflection is the phenomenon by which light incident on a surface is re-emitted, possibly in different directions. There are two types of reflections considered here: specular and diffuse. In specular reflection, a collimated beam of light on a surface reflects into another collimated beam of light. The angle between the incident ray and the normal vector is equal to the angle between the reflected ray and the normal vector. Furthermore the incident beam, the normal to the surface and the reflected beam are in the same plane. In contrast, a beam of light can reflect diffusively into many beams propagating in many different directions. Reflection of solar UV radiation on satellite surfaces can be important whenever the reflected light can reach another surface element. This then leads to enhanced solar illumination on surfaces already exposed to direct solar radiation, or to illumination on elements which would otherwise not be exposed to UV radiation at all. In either case the result is an enhancement of emitted photoelectrons by satellite components. The new reflection solar illumination model implemented in PTetra can also account for the albedo α, or reflectivity of materials whereby the energy reflected by a surface triangular element is α times the incident energy.

3.4.1 Specular reflection

Consider an incident ray reflected as shown in Fig. (3.8), where $\hat{n}$ is the normal vector to the surface, $\hat{u}$ and $\hat{\rho}$ are the incident and reflected ray vectors respectively.

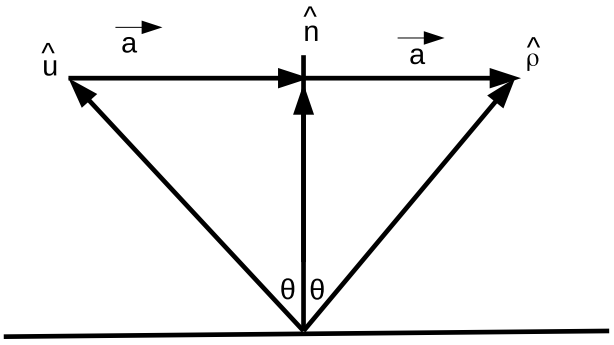

Figure 3.8: Illustration of the unit vector $\hat{u}$ pointing toward the Sun and the unit vector $\hat{\rho}$ pointing in the direction of a ray reflected specularly.

From the relations

$$\hat{\rho} = \hat{n}cos\theta + \vec{a} \tag{3.4}$$

$$\hat{u} + \vec{a} = \hat{n}cos\theta \tag{3.5}$$

$$cos\theta = \hat{n}.\hat{u},$$

it can be seen that

$$\vec{a} = \hat{n}(\hat{n}.\hat{u}) - \hat{u} \tag{3.6}$$

and

$$\hat{\rho} = 2(\hat{n}.\hat{u}).\hat{n} - \hat{u}. \tag{3.7}$$

At the beginning, the reflection vector $\hat{\rho}$ is calculated, from a beam $\hat{u}$ that has direct illumination and pointing toward the Sun as shown in equation (3.7). Once $\hat{\rho}$ is calculated it is considered to be the new direction in which solar radiation propagates. If incident on another surface, the illumination of that surface element is incremented, and the process is repeated. Whenever a reflected ray reaches the outer boundary the ray is considered to escape the simulation domain, and the iterations stop. The cross section of the illuminated area is defined as the absolute value of the dot product between the unit vector perpendicular to the area and the unit vector pointing in the direction of the light ray, multiplied by the surface

area.

In some cases such as shown in Fig. (3.9), the cross section of the incident beam might be different from the cross section of that beam on the receiving triangle. For example, in the right side of Fig. (3.9) the cross section of the incident beam A_1 is larger than the cross section of the beam B_1 on the receiving triangle. In this case, only a fraction of the radiation incident on surface B_1 is accounted for, and it is that fraction of the incident radiation which is considered when accounting for the light reflected from the smaller element B_1. On the left side of Fig. (3.9), the cross section of the incident beam A_2 is smaller than the cross section of the receiving area B_2. In this case the full amount of light of the incident beam is received by the surface with the larger cross section.

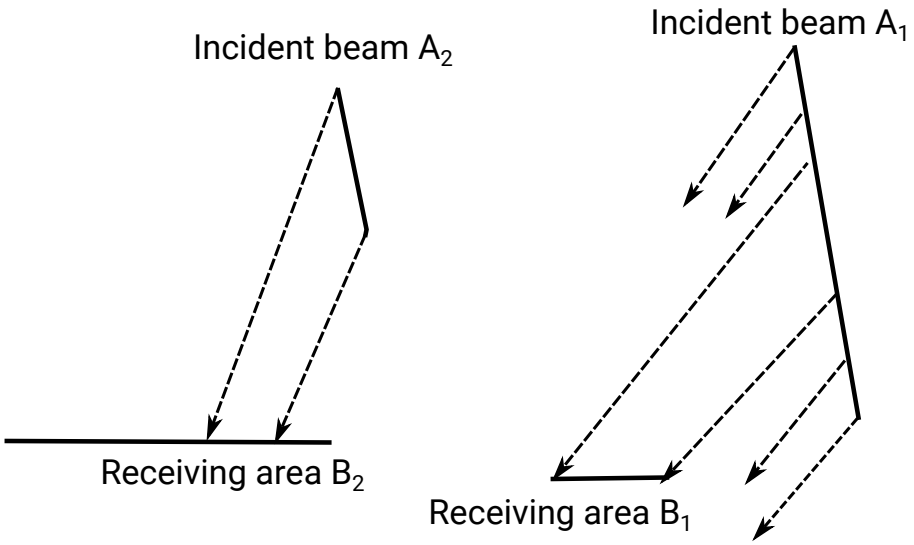

Figure 3.9: Illustration of the cross section of a surface area illuminated by a light beam.

3.4.2 Diffuse reflection

For diffuse reflection, the incident light can be reflected in many directions with different angles. For a given incident light ray a single reflected ray is generated with a random angle θ between the direction of propagation and the normal to the surface. This angle is in the range between $(0, \pi/2)$. A random azimuthal angle ϕ

ranging from $(0, 2\pi)$ is also used to complete the definition of the direction of the reflected light as shown in Fig. 3.10.

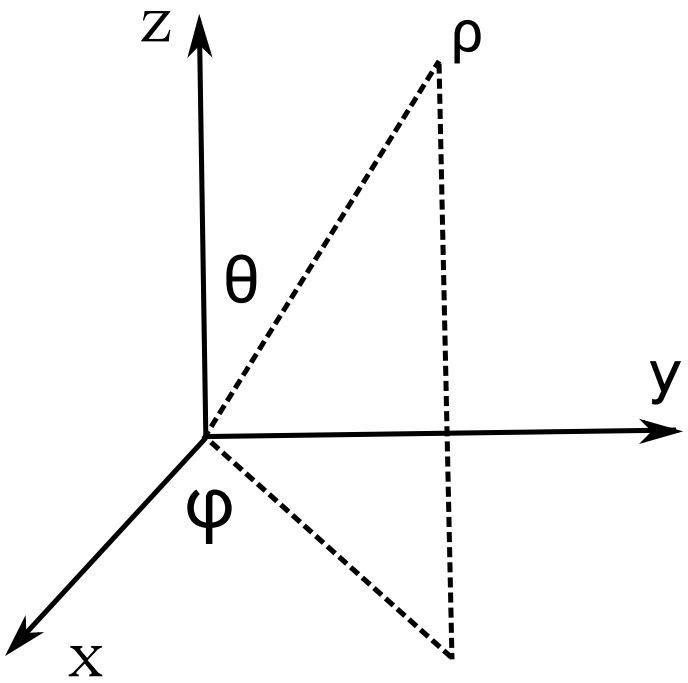

Figure 3.10: Illustration of the geometry used in calculating diffuse reflection.

The two angles θ and ϕ are defined as follows:

$$\theta = \cos^{-1} A_1 \tag{3.8}$$

$$\phi = 2\pi A_2 \tag{3.9}$$

where A_1 and A_2 are random numbers from 0 to 1 and

$$\hat{\rho} = \sin\theta\cos\phi\hat{x} + \sin\theta\sin\phi\hat{y} + \cos\theta\hat{z} \tag{3.10}$$

where $\hat{x}$, $\hat{y}$ and $\hat{z}$ are normalized vectors in the plane of the reflecting surface, and perpendicular to it respectively.

Chapter 4

Example simulations and results

Simulations of solar illumination and multiple reflections were done by using the three dimensional code PTetra which is summarized in Chapter 1 and for which a detailed description of the code is given in [38]. The code uses unstructured tetrahedral meshes to represent complex structures. It is generated with gmsh. PTetra uses a PIC approach, in which macro particles carry a statistical weight equal to the ratio between the actual number of particles in a plasma, to the number of "macro particles" considered in the simulation. It accounts for satellite interaction with the plasma accounting for such processes as satellite charging, photoelectrons and secondary electrons emission.

4.1 An idealized satellite geometry

In this section results are presented for an idealized geometry constructed specifically to illustrate multiple reflections. A detailed description of the idealized geometry was introduced in section (3.2). For simplicity, no background plasma is assumed when looking at photoelectron emission. In all cases considered an albedo of 0.9 is assumed when considering reflections, and the direction toward the Sun is given by $\vec{u} = (1,\ 0.2,\ 0.3)$

4.1.1 Direct illumination

Figure (4.1) shows a distribution of collected current density associated with photoelectron emission. We note that photoelectron emission leads to negative current emitted per unit surface area, or equivalently, to a positive collected current density. This is why the figure shows positive current density collected on surface elements in these illustrations. We also note that collected current density calculated on each triangular surface element is not perfectly constant on a given surface. The small variations between triangles are caused by statistical errors and the finite number of electrons used in the simulation of emitted photoelectrons.

The first case considered is obtained with the ray tracing approach in which a single ray, starting from each triangle centre, is traced in the direction of the Sun, as described in section (3.3.2). We recall that with this approach, a triangle is fully lit when the ray reaches the outer boundary of the simulation domain, or not at all when it intersects a structure before reaching the boundary. This is clearly seen from the lower right panel in Fig. (4.1) where triangles are either red (emitting electrons) with approximately the same intensity, or blue (not emitting). The illumination pattern calculated in this case is identical to what would be obtained with the original PTetra stepping strategy.

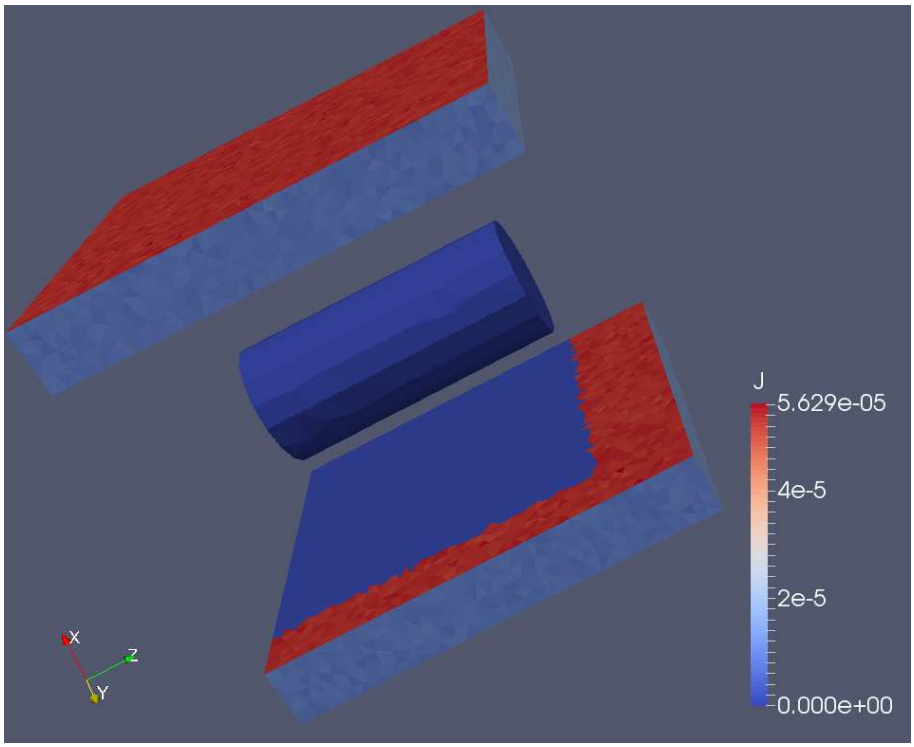

Figure 4.1: Illumination pattern computed with the original PTetra stepping algorithm, using only one ray per triangle. Current densities J are in units of $\mathrm{A/m^2}$.

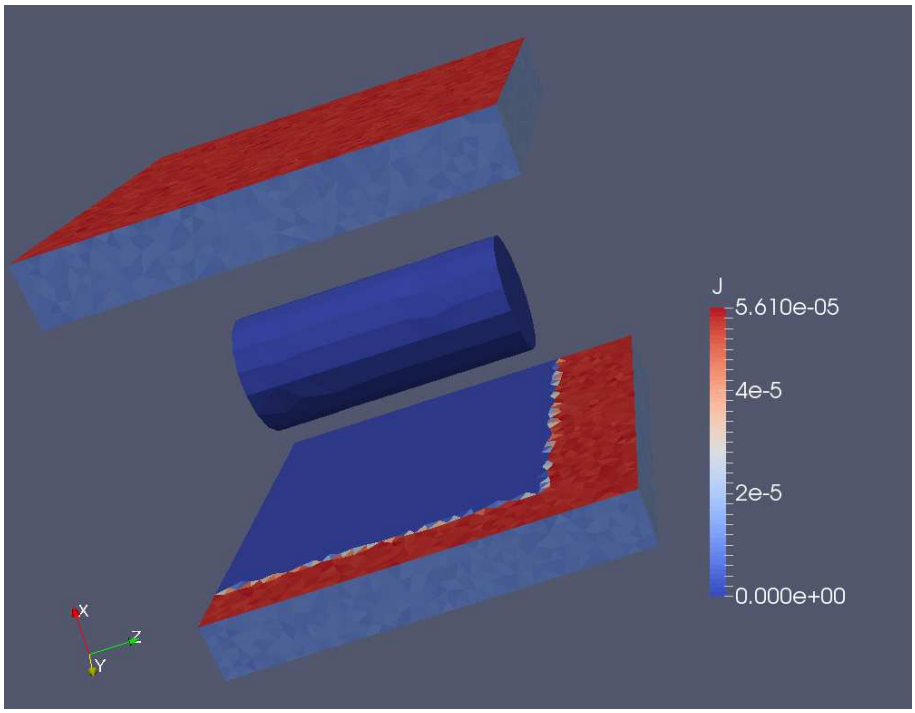

Figure 4.2: Illumination pattern computed when using multiple points per triangle from direct illumination only.

Figure (4.2) shows results from a simulation in which many points are traced toward the Sun, in each triangle. The number of points traced from each triangle is proportional to the surface area of each triangle, and the proportionality constant is set by the user. In this example 25 points were used for the triangle with the smallest surface area. In this case, some rays will intercept other structures, while others reach the outer boundary without going through any physical structure. The fraction of rays which reach the outer boundary to the total number of rays considered is proportional to the illumination, and photoelectron emission attributed to a given triangle. The band of partially illuminated triangles is clearly visible in the lower right panel in the figure.

4.1.2 100% Specular reflection

The manifestation of multiple reflections is clearly visible in Fig. (4.3) where the illumination pattern seen in Fig. (4.2) is still visible, but where several other

illumination patterns appear as a result of light being reflected back and forth between the structures. The patterns seen in the figure are readily understood in terms of these multiple reflections. For example the oval shape on the top left slab in the lower panel is associated with light reflected on the opposite rectangular prism, incident on the flat top of the cylinder, and reflected again on the opposite rectangular prism. We also note that some triangles emit more photoelectrons than the maximum emitted current density calculated without multiple reflection (see Fig.4.2). This is due to the fact that multiple reflections cause certain triangles to be illuminated by reflecting rays more than once. Finally we note that reflection of light from the cylinder leads to somewhat spotty patterns, particularly on the upper left block in the lower panel. This is due to the fact that the cylinder is represented with finite size triangles rather than as a smooth surface. A higher mesh resolution (smaller triangles) here would lead to smoother looking reflection patterns.

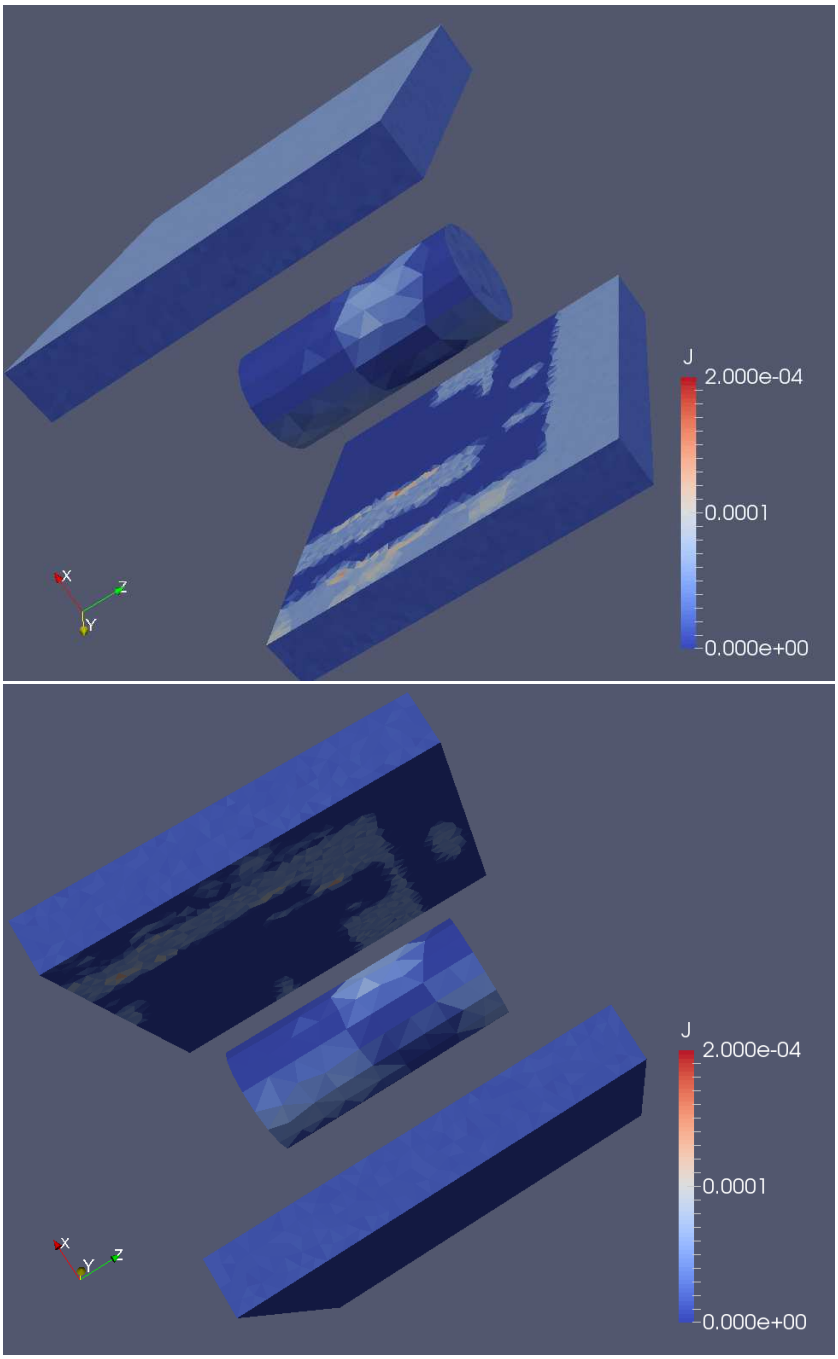

Figure 4.3: Illumination pattern computed when using multiple points per triangle with multiple reflections, assuming 100% specular reflection.

4.1.3 Combination of specular and diffuse reflection

Figure (4.4) shows illumination patterns obtained with half specular and half diffuse reflection. Here essentially the same patterns are seen as in the case with 100 % specular reflection Fig. (4.3), except that in this case: i) the maximum collected current is less than with 100 % specular reflection, and ii) we see photoelectron emission in parts of the surface where there was none when reflection was purely specular. The lower collected current is understandable from the fact that with half diffuse reflection, a fraction of the reflected light that would be incident on other structures will in fact be directed between structures and not add to the illumination of other structures. Here also we observe areas where illumination is enhanced due to multiple illuminations, but the maximum values of collected current density are less than when reflection is purely specular.

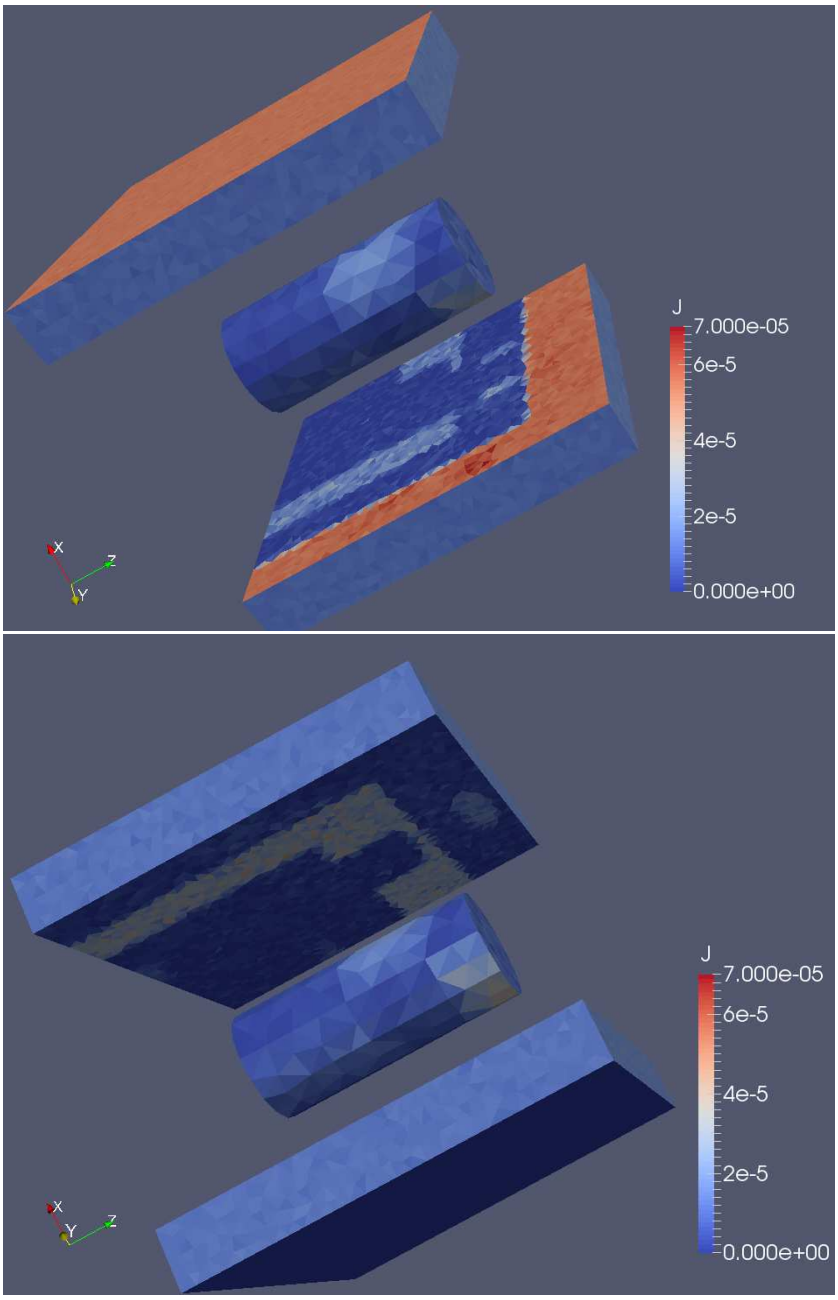

Figure 4.4: Illumination pattern computed when using multiple points per triangle with multiple reflections assuming 50% specular and 50% diffuse reflection.

4.1.4 100% diffuse reflection

Finally we consider a case in which reflection is purely diffusive. In the result shown in Fig. (4.5) essentially all the patterns seen in Figs.(4.3)and (4.4) obtained

with full and partial specular reflection have disappeared. Multiple reflections lead to weak and approximately uniform illumination on areas not directly illuminated by the Sun. The bands subject to direct illumination on the lower block in the top panel of the figure show slightly higher emission than in the absence of multiple reflections. Also due to the finite number of rays used to simulate diffuse reflection, statistical variations in the magnitude of photoelectron emission is clearly larger than with direct illumination only (c.f. Fig. 4.2).

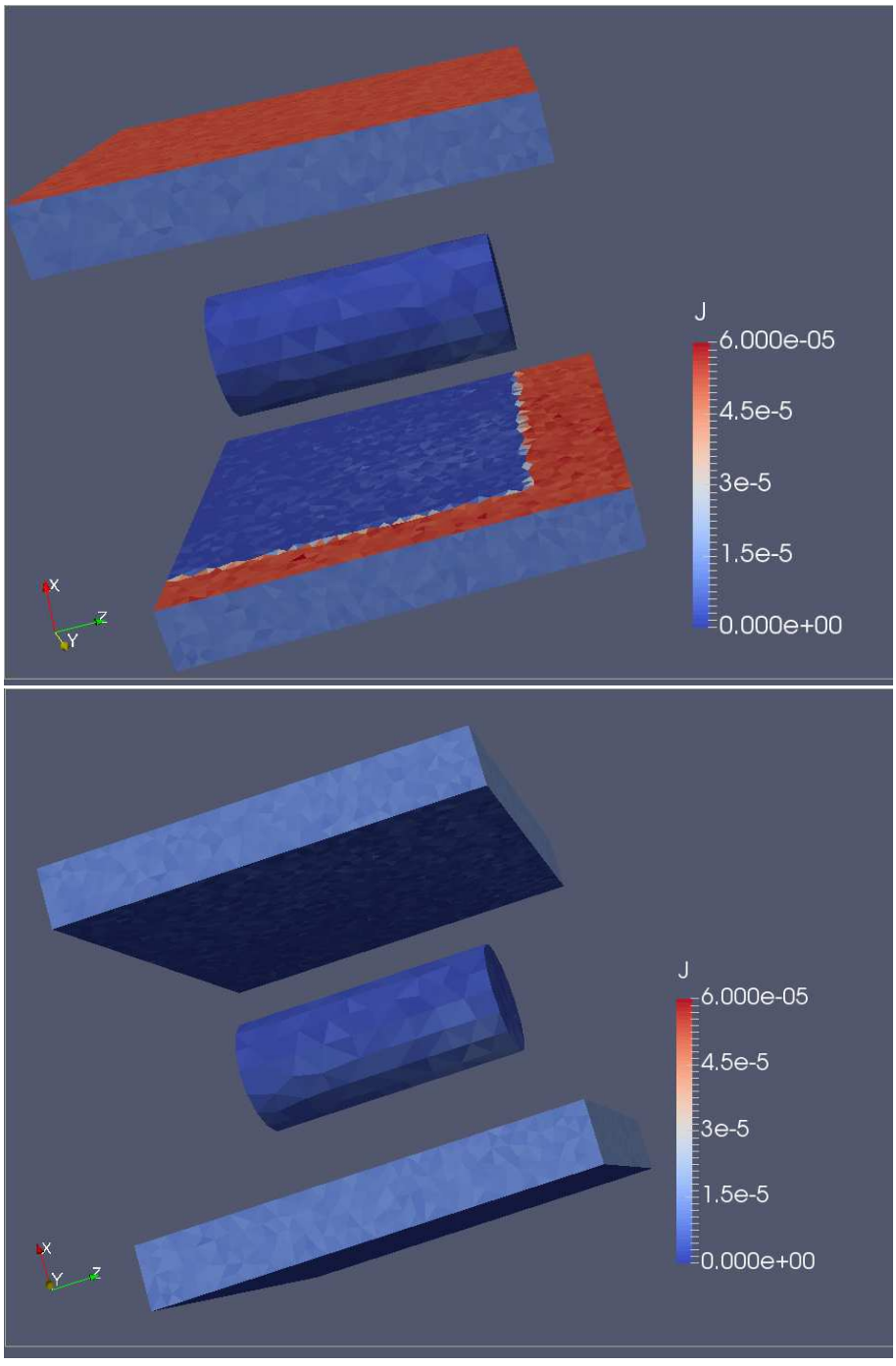

Figure 4.5: Illustration of the collected current density when multiple reflections are taken into account with 100% diffuse reflection.

4.2 More realistic geometry

Simulation results obtained with a more realistic satellite component geometry are now presented. The component considered approximates the vector magnetometer star tracker assembly on the Swarm satellites. For brevity, these will be referred to as the "assembly" in what follows. The three Swarm satellites were launched in 2013. The satellite length is approximately 10m. They were deployed for the purpose of measuring Earth magnetic fields with very high accuracy [39]. Figure (4.6) illustrates the full length of the satellite and its main instruments. Simulating the entire spacecraft under realistic ionospheric conditions would be too time consuming for the purpose of this thesis, so only the optical bench and vector magnetometer assembly are considered in what follows. The mesh resolution was chosen to show the main geometrical variation of the object, but was not optimized for the purpose of simulating the interaction of plasma. It was for the purpose of illustration of solar Illumination and multiple reflections. Two sets of simulations are considered, corresponding to illumination and photoelectron emission calculated a) without, and b) with a plasma background. In all cases considered, the direction toward the Sun is given by $\vec{u} = (1, 1, 1)$.

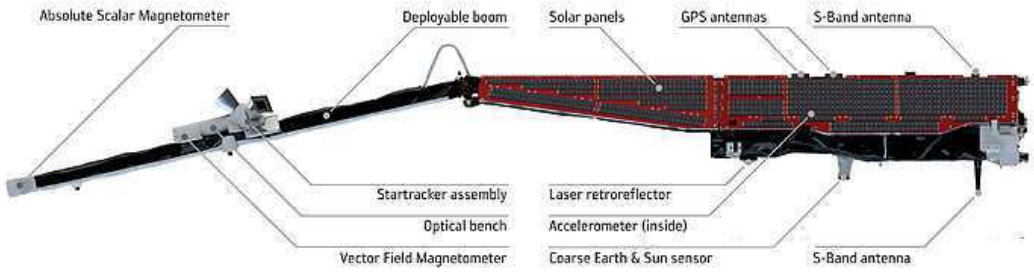

Figure 4.6: Illustration of a Swarm satellite with several of its main instruments. The length of the satellite is approximately 10 m.
(http://www. geomag.bgs.ac.uk/education/swarm_overview.html)

4.3 Simulations made without a plasma background

4.3.1 Direct illumination

Figure (4.7) shows a map of emitted photoelectron current density when only direct illumination is considered; that is, when multiple reflection is ignored. Here and in what follows, we use many points per triangular surface elements as described in section (3.3.2) in order to account for the possibility of partial illumination of triangles.

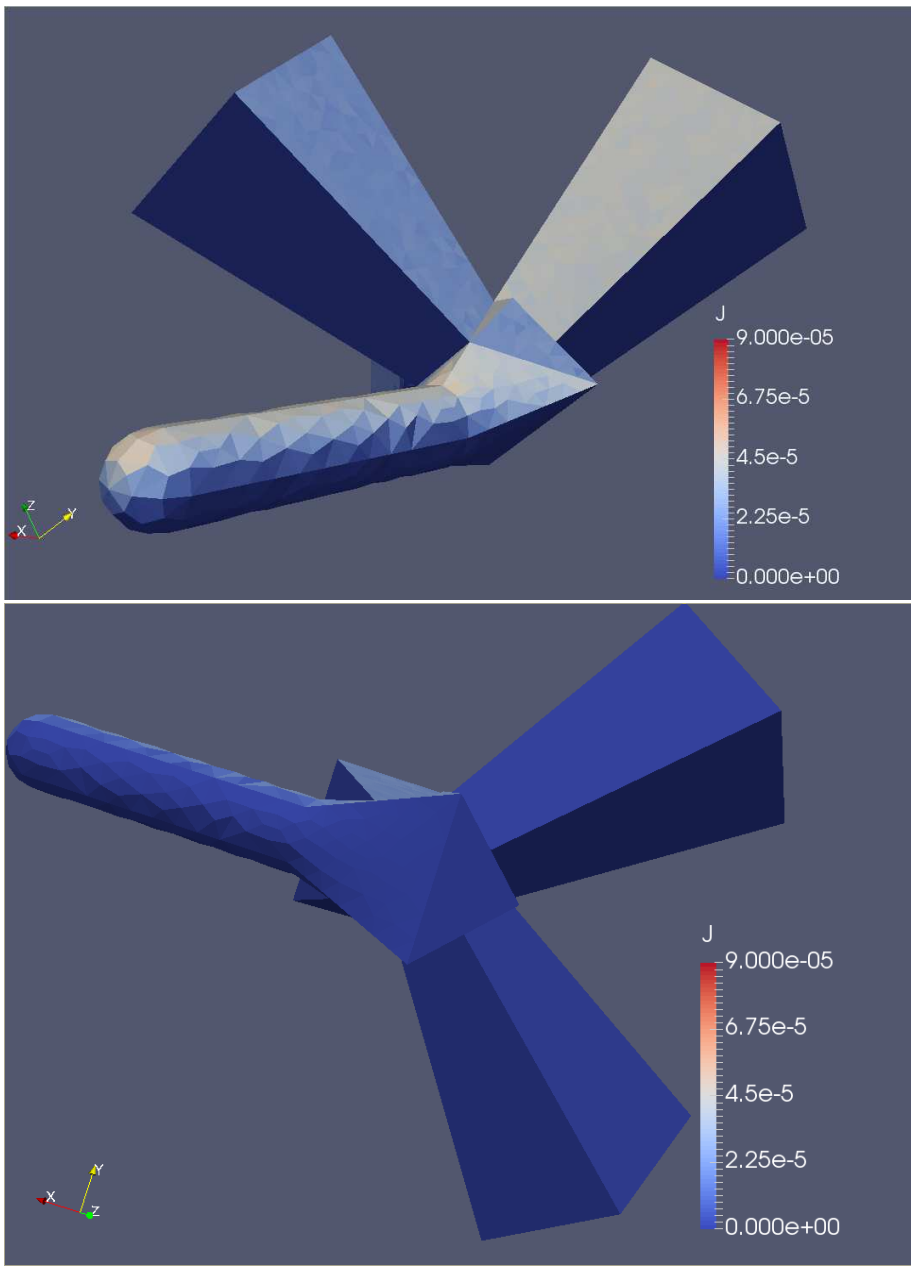

Figure 4.7: Illumination map of the Swarm optical bench - magnetometer assembly computed with direct illumination only. The scale length of this assembly is approximately 70 cm.

4.3.2 100 % specular reflection

Figure (4.8) shows the illumination map calculated with multiple reflections assuming 100% specular reflection. With this geometry and the direction of the Sun,

the number of reflections which result in other surface elements being illuminated is limited to one or at most two.

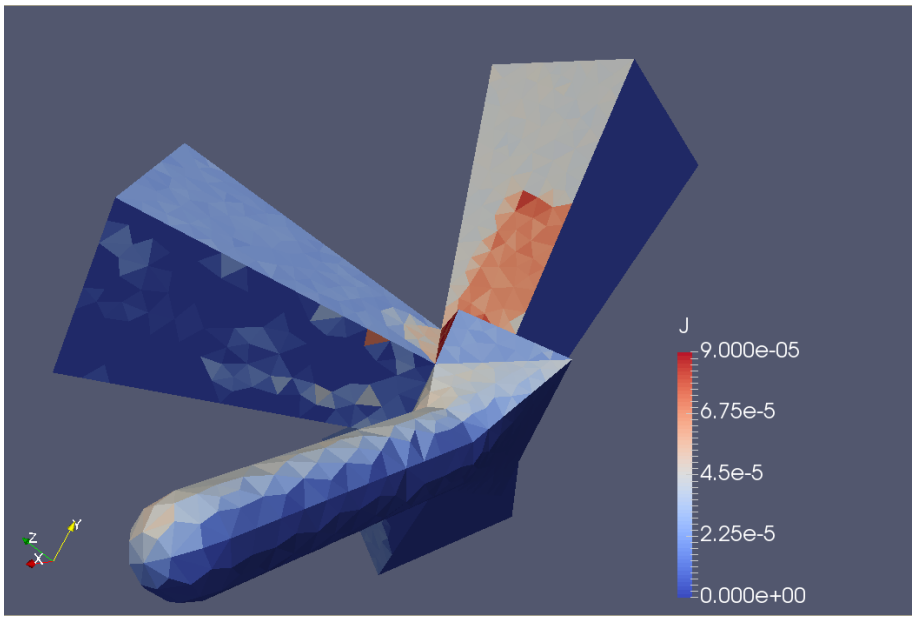

Figure 4.8: Illumination map of the Swarm optical bench - magnetometer unit computed with 100% specular reflection.

4.3.3 Combination of specular and diffuse reflection

Figure (4.9) shows the illumination map calculated when reflection is half specular and half diffuse. Basically the same patterns of reflected light can be seen as with 100% specular reflection, but with attenuated intensities. This is similar to what was found with the idealized geometry when comparing illumination patterns obtained with fully specular and partly specular reflection.

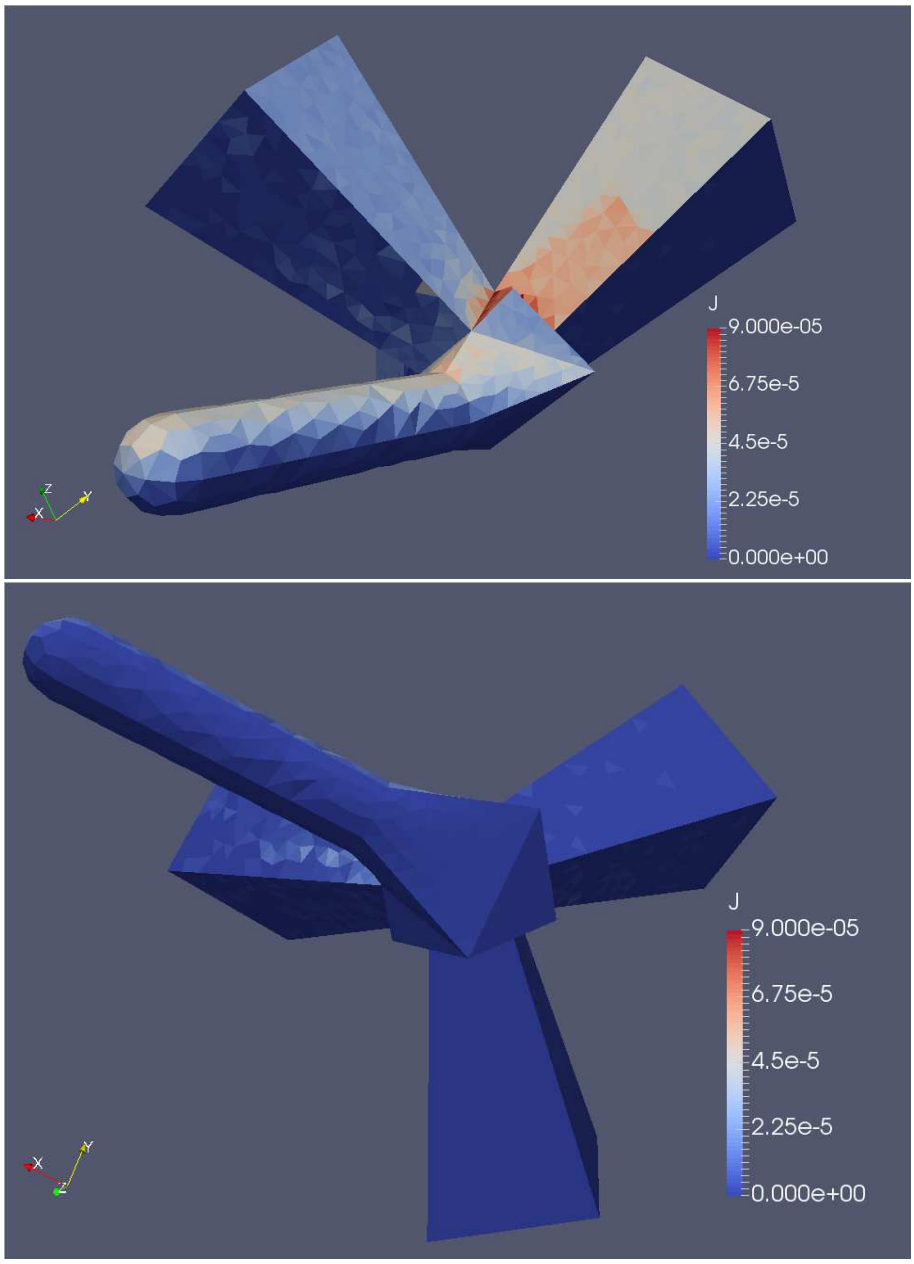

Figure 4.9: Illumination map of the Swarm optical bench - magnetometer unit computed with 50% specular and 50% diffuse reflection.

4.4 Simulations made with a plasma background

We now consider simulation results obtained with the same geometry but in the presence of a plasma background. The effects of multiple reflections are illustrated

in three cases, calculated with a) direct illumination only (no multiple reflection), b) multiple reflections taken into account with 100% specular reflection, and c) multiple reflections with half specular and half diffuse reflections. In each case we show the profile of current density collected at the surface of the assembly, which is now caused by a combination of photoelectron emission and a collection of plasma particles. We also show cross sections of the plasma current density caused by photoelectron emission and plasma interaction with the assembly, and the resulting perturbed magnetic field. The importance of multiple reflections is assessed by comparing illumination maps, plasma current densities and resulting perturbed magnetic fields computed with and without multiple reflections. The plasma parameters used in the simulations are summarized in Table (4.1).

Table 4.1: Plasma parameters assumed in the simulations

Physical Parameter	Numerical value
Electron density	1×10^{10} m^{-3}
Electron temperature	4.0 eV
Ion species	H^+
Ion density	1×10^{10} m^{-3}
Ion temperature	4.0 eV
Ion mass	1.66×10^{-27} kg
Background magnetic field	(35 , 10 , 0) μ T
Electron thermal velocity $v_{the} = \sqrt{\frac{2kT_e}{m_e}}$	1.19×10^6 m/s
Electron thermal gyro-radius $\frac{v_{the} m_e}{eB}$	0.187 m
Ion thermal velocity $v_{thi} = \sqrt{\frac{2kT_i}{m_i}}$	2.78×10^4 m/s
Ion thermal gyro-radius $\frac{v_{thi} m_i}{eB}$	7.713 m
Debye length $\sqrt{\frac{\epsilon_0 kT}{n_e e^2}}$	0.148 m

4.4.1 Direct illumination

Figure (4.10) shows the collected current density calculated when direct solar illumination only is taken into account (no multiple reflections). Cross sections of the corresponding plasma current density are shown in Fig. (4.11). Given the computed current densities associated with spacecraft-plasma interaction, it is interesting to use the Biot-Savard law to calculate the associated perturbed magnetic field. Cross sections of the x, y, z components of this field are shown in Fig. (4.12). The current densities and resulting magnetic field perturbation are very small in this case; of order of 10 pT for the magnetic field magnitude. Referring to Figs. (4.11) and (4.12) it is interesting to note that the positive x component (directed to the right) of the perturbed magnetic field is consistent with the current density layers going into the page above the spacecraft and out of the page below it.

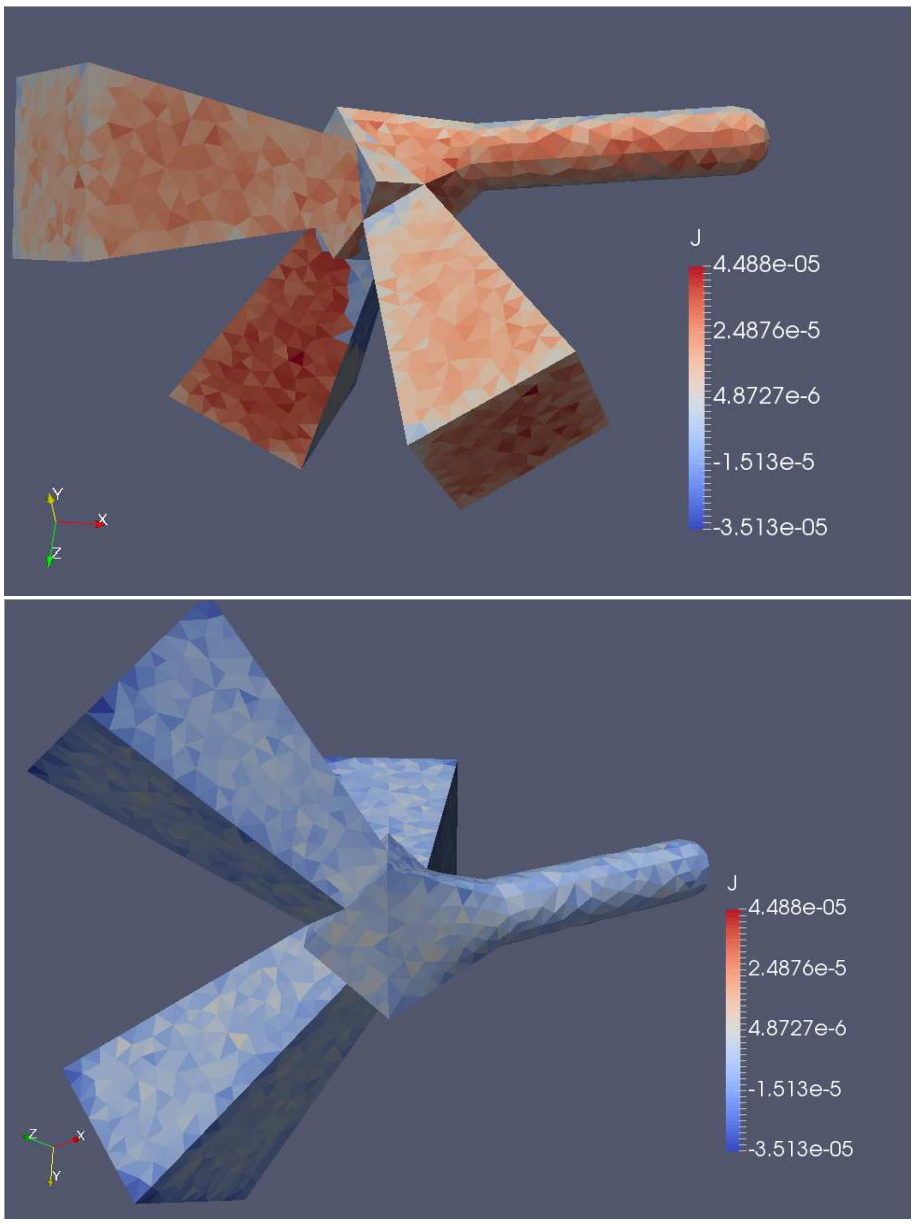

Figure 4.10: Collected current density on the Swarm optical bench - magnetometer unit computed with plasma and direct illumination only.

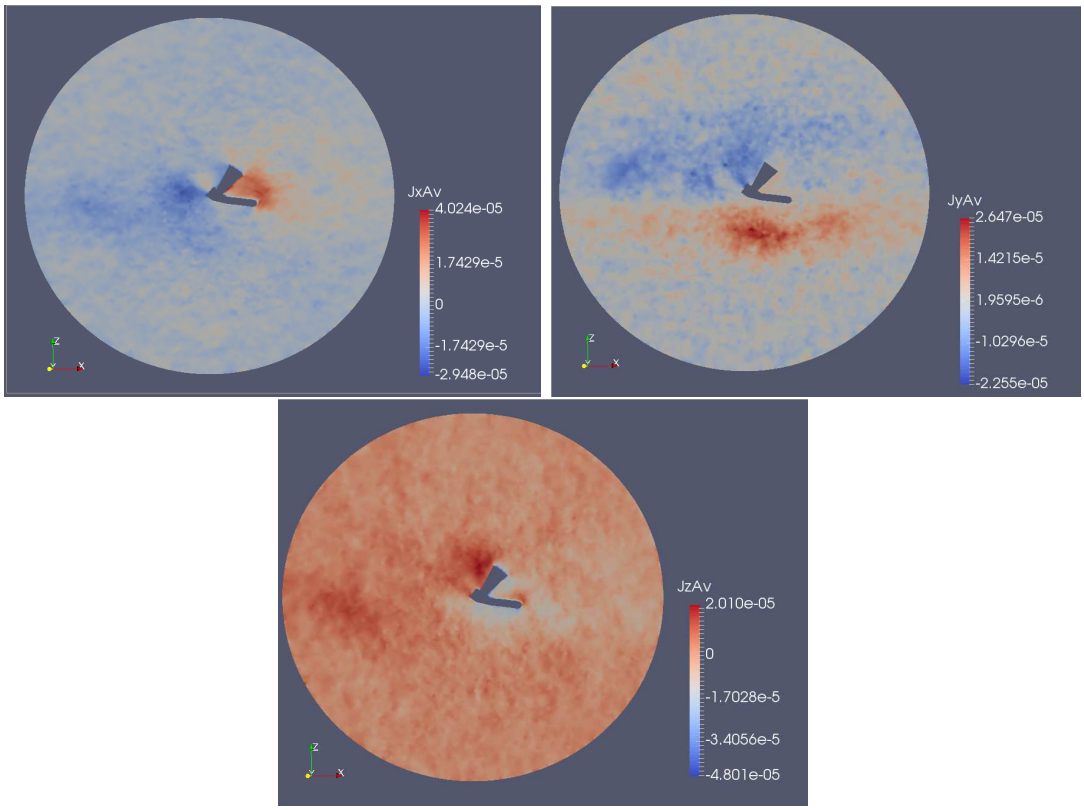

Figure 4.11: Cross sections of the average current densities in x, y and z directions computed with direct illumination.

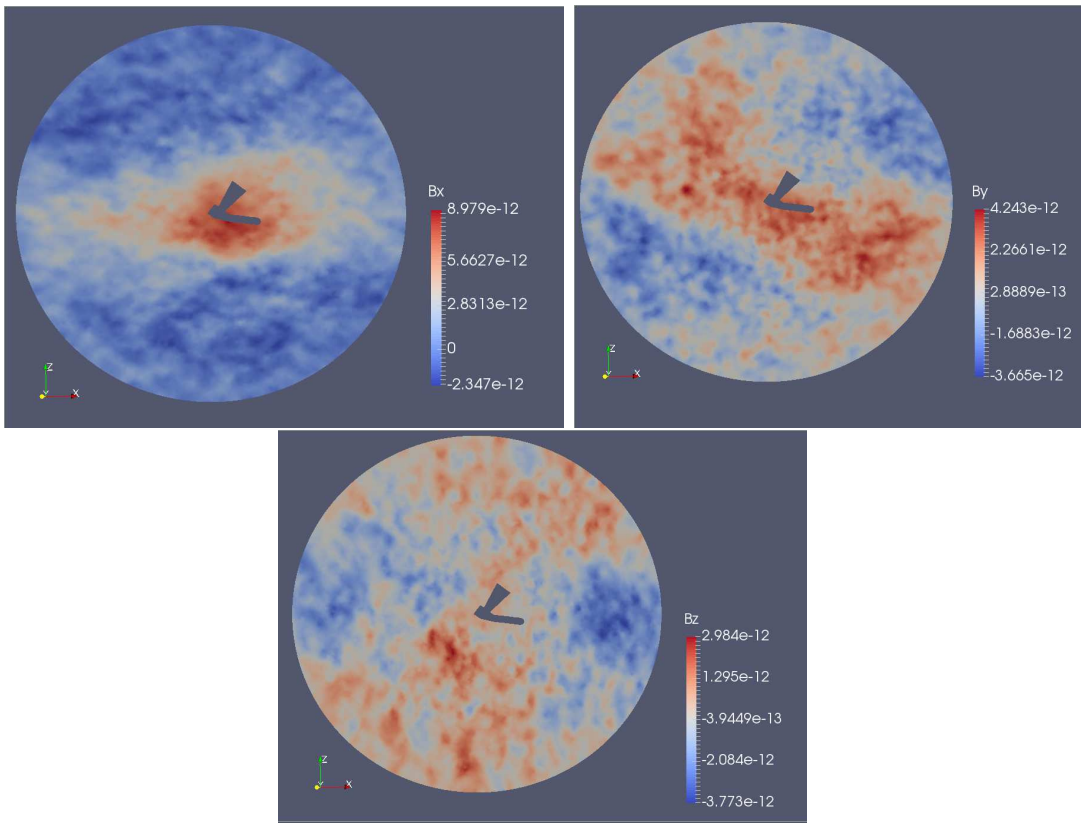

Figure 4.12: Cross section s of the perturbed magnetic field in the x, y and z directions computed with direct illumination.

4.4.2 Specular reflection

Similar results are now presented in Fig. (4.13) to (4.15) when multiple specular reflections are taken into account. Emitted photoelectron patterns are attenuated by collected current surface density associated with background plasma. Here again we find current into the page above the structure and out of the page below it, which leads to a positive (to the right) x component of the perturbed magnetic field. In this case the magnitudes of the components of the current density in the plasma surrounding the spacecraft and their spatial profiles are comparable to those computed without multiple reflections.

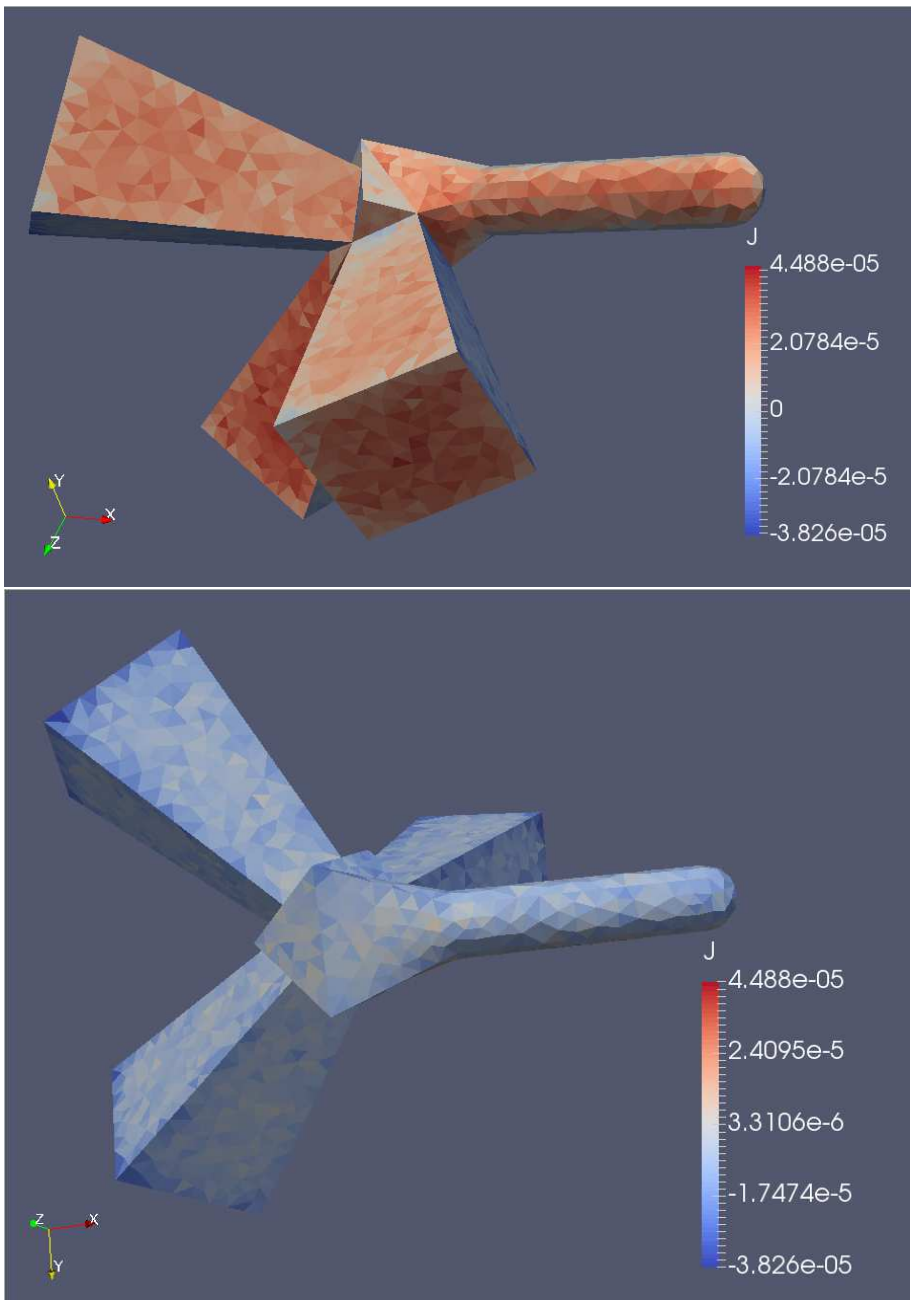

Figure 4.13: Collected current density computed with 100% specular reflection on the Swarm optical bench - magnetometer unit, while accounting for a background plasma.

4

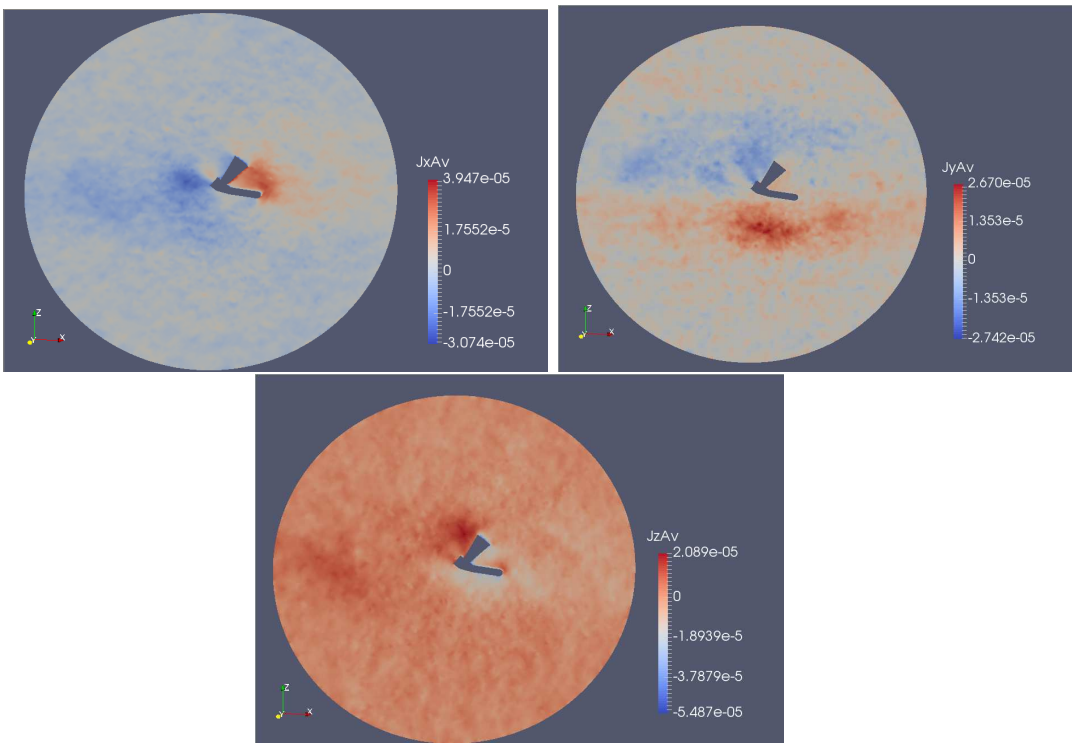

Figure 4.14: Cross sections of the average current densities in x, y and z directions computed with 100% specular reflection with plasma.

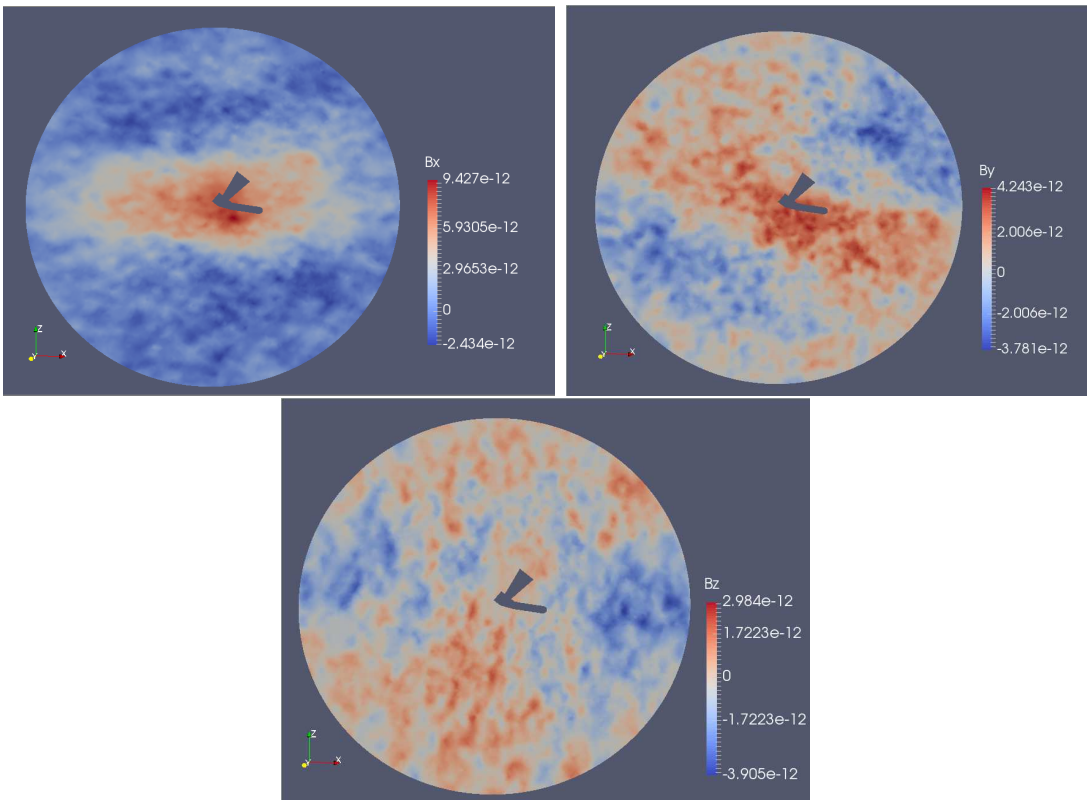

Figure 4.15: Cross section s of the perturbed magnetic field in the x, y and z directions computed with 100% specular reflection with plasma.

4.4.3 Specular and diffuse reflection

Finally, Figs. (4.16) to (4.18) show results obtained in the presence of a background plasma, with multiple reflections assuming 50% specular and 50% diffuse reflection. In this case, the numerical values of the components of the current density and perturbed magnetic field are different, but their spatial distribution is seen to be similar to that computed with direct illumination only (Figs. 4.11 and 4.12). Referring to table 4.2, the relative differences of the maximum current densities and the maximum and the minimum values of the perturbed magnetic field for all cases considered (direct illumination, 100% specular and 50% / 50%) are approximately 5% or less. The largest relative differences are found for the minimum current densities, which are of order 10%. The assembly floating potentials computed in the three cases considered are identical four significant figures.

These relative differences are not considered to be significant considering other uncertainties such as albedos, angular distributions of diffusively reflected radiation, and photoelectron emission rates used in the simulations.

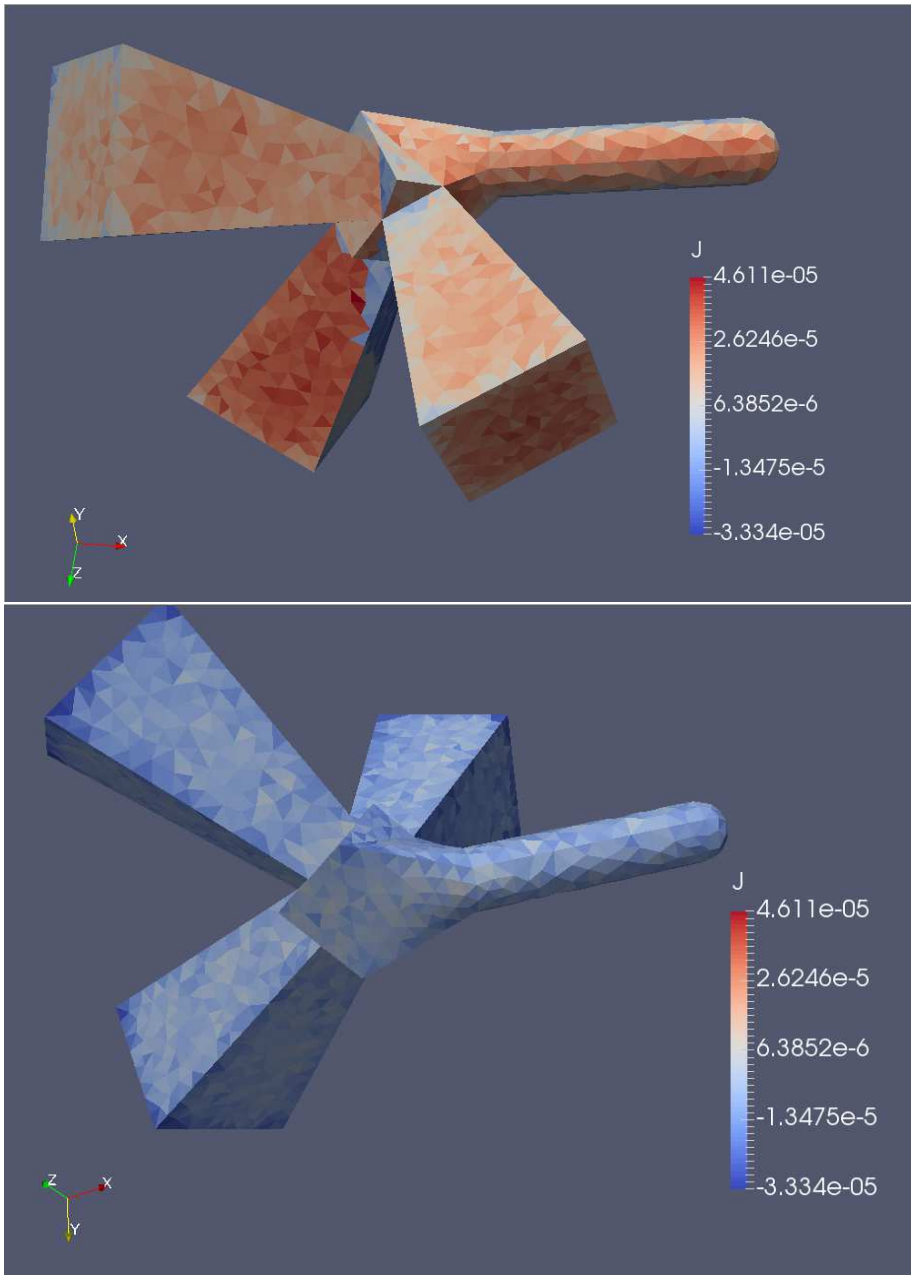

Figure 4.16: Collected current density on the Swarm optical bench - magnetometer unit computed with 50% specular and 50% diffuse reflection in the presence of plasma.

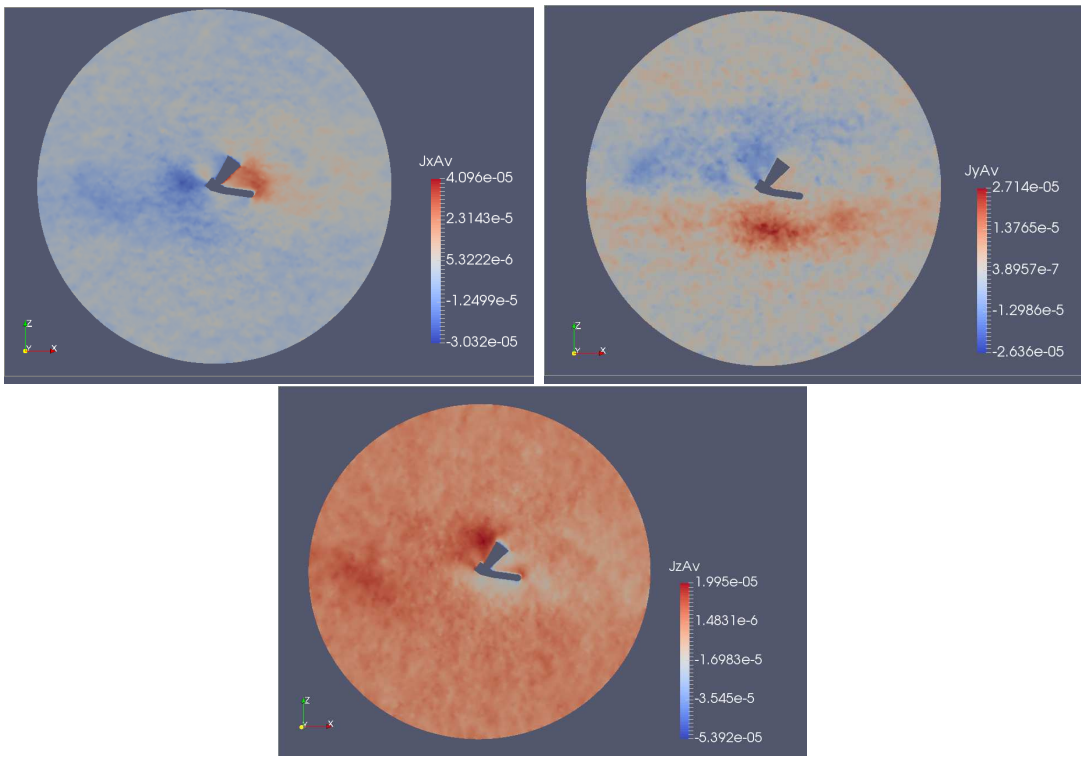

Figure 4.17: Average current densities in x , and z components computed with 50% specular and 50% diffuse reflection.

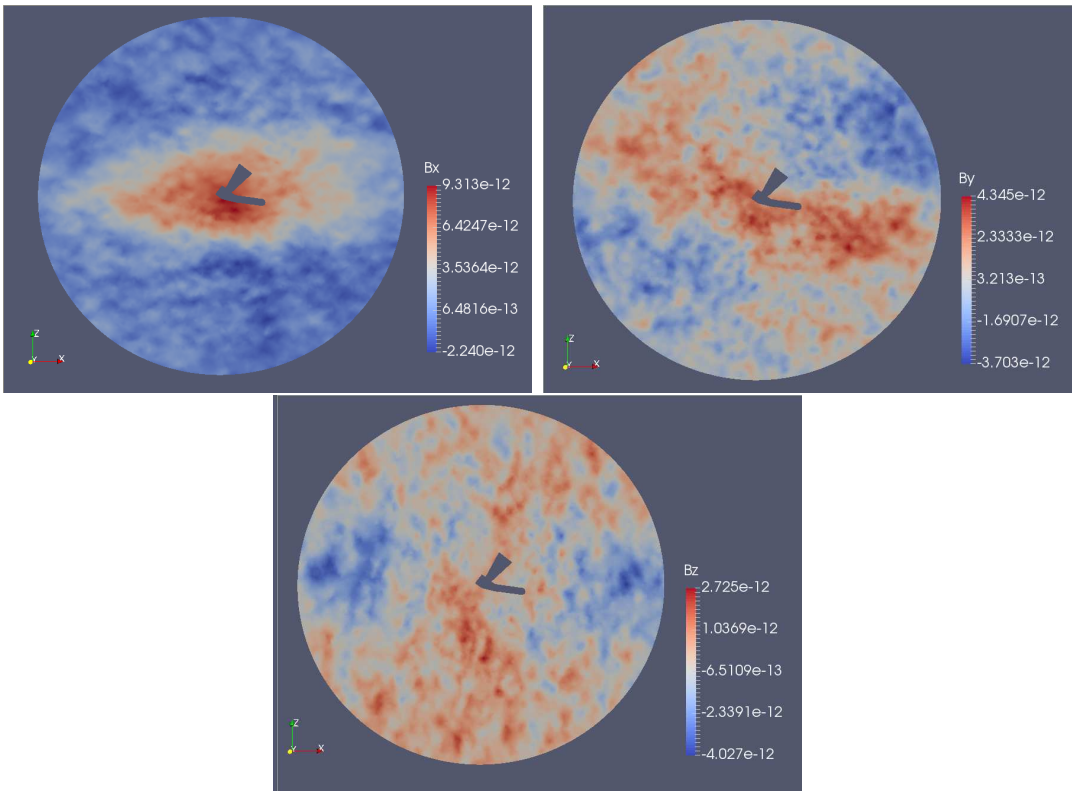

Figure 4.18: Cross section s of the perturbed magnetic field in the x, y and z components computed with direct illumination.

Table 4.2: Quantitative comparison between results obtained with different types of illumination

Type of illumination	Direct illumination	100% specular	50% / 50%
floating potential	-7.752 V	-7.752 V	-7.752 V
$J_{max(x,y,z)}$ $(\frac{\mu A}{m^2})$	(40.2, 26.4,20.20)	(39.4, 26.7,20.8)	(40.9,27.1,19.9)
$J_{min(x,y,z)}$ $(\frac{\mu A}{m^2})$	(-29.4,-22.5,-48.01)	(-30.7,–27.4,–54.8)	(-30.3,-26.3,-53.9)
$B_{max(x,y,z)}$ (pT)	(8.97,4.24,2.34)	(9.42,4.24,2.98)	(9.31,4.34,2.72)
$B_{min(x,y,z)}$ (pT)	(-2.34,-3.66,-3.77)	(-2.43,-3.78,-3.90)	(-2.42,-3.70,-4.02)

Chapter 5

Summary and conclusion

Simulation results for two cases of plasma satellite interactions have been presented in this thesis, corresponding to direct illumination and multiple reflections. These were simulated using the computational model PTetera based on an electrostatic time-dependent particle in cell (PIC) approach. A distinctive feature of PTetra is that it accounts for a background magnetic field, and it uses an unstructured adaptive mesh to represent the simulation domain. This enables a realistic representation of structures with complex shapes, and the imposition of physical boundary conditions. The main contribution of this study was to improve the calculation of solar illumination in PTetra, for the purpose of better simulating photoelectron emission. This was done by:

- replacing the original stepping strategy for determining surface illumination, with a more reliable ray tracing approach,
- improving the accuracy of solar illumination by accounting for partial illumination of surface triangular elements, and
- adding an option in the code to account for multiple reflections between surface elements with an arbitrary combination of specular and diffuse reflections.

Simulations were made by considering an ideal satellite geometry and a more realistic geometry representing the optical bench of the Swarm satellites. The idealized geometry is used to clearly illustrate the effects of multiple reflections of incident solar radiation. These can enhance solar illumination on satellite surfaces directly exposed to solar radiation, or produce illumination on elements which would otherwise not be exposed to UV radiation at all. The effect of multiple reflections on plasma currents and resulting perturbed magnetic fields is considerably weaker than that associated with the interaction of surfaces with the background plasma when such effects from a plasma are taken into account. It is therefore concluded that multiple reflection effects on photoelectron emission and currents generated by satellite-environment interaction, are relatively unimportant in the presence of plasmas with densities corresponding to those encountered in the ionosphere. Multiple reflections however, should be more significant in lower density plasmas such as those encountered in the solar wind.

5.1 Future work

This thesis presents improvements to the algorithm used for calculating photoelectron emission in PTetra. The main improvement consists of accounting for partial illumination of surface triangular elements, and multiple reflections of solar radiation on spacecraft components. In the calculations considered here, for simplicity, the Sun was treated as point source, a constant albedo was assumed for all surfaces and diffuse reflection was assumed to be isotropic. Further improvements to the model should include:

- a finite width of the solar disk,
- the use of tabulated albedos for different materials, and
- a more physical model for diffuse reflection, accounting for a) the angle at which incident radiation reaches a surface, and b) the angular distribution

of reflected light depending on the angle of incidence and surface material properties.

Bibliography

[1] Yohsuke Kamide and Abraham C-L Chian. *Handbook of the solar-terrestrial environment*. Springer Science & Business Media, 2007.

[2] Shu T Lai. *Fundamentals of Spacecraft Charging: Spacecraft Interactions with Space Plasmas*. Princeton University Press, 2011.

[3] Tadanori Ondoh and Katsuhide Marubashi. *Science of space environment*. IOS Press, 2001.

[4] John K Hargreaves. *The solar-terrestrial environment*. Cambridge University Press, 1992.

[5] Wolfgang Baumjohann and Rudolf A Treumann. *Basic space plasma physics*. World Scientific, 1997.

[6] Robert D Hunsucker and John Keith Hargreaves. *The high-latitude ionosphere and its effects on radio propagation*. Cambridge University Press, 2007.

[7] Vladimir Bychkov, Gennady Golubkov, and Anatoly Nikitin. *The Atmosphere and Ionosphere: Dynamics, Processes and Monitoring*. Springer Science & Business Media, 2010.

[8] Erdal Yiğit. *Atmospheric and Space Sciences: Neutral Atmospheres*, volume 1. Springer, 2015.

[9] Danny Summers, Ian R Mann, Daniel N Baker, and MG Schulz. *Dynamics of the Earth's radiation belts and inner magnetosphere*, volume 199. John Wiley & Sons, 2013.

[10] Janet L Barth. Space and atmospheric environments: from low Earth orbits to deep space. In *Protection of Materials and Structures from Space Environment*, pages 7–29. Springer, 2004.

[11] George K Parks. Physics of space plasmas-an introduction. 1991.

[12] José A Bittencourt. *Fundamentals of plasma physics*. Springer Science & Business Media, 2013.

[13] Francis F Chen and Schweickhard E von Goeler. Introduction to plasma physics and controlled fusion volume 1: Plasma physics. *Physics Today*, 38: 87, 1985.

[14] Daniel Hastings and Henry Garrett. *Spacecraft-environment interactions*. Cambridge University Press, 2004.

[15] Elden C Whipple. Potentials of surfaces in space. *Reports on Progress in Physics*, 44(11):1197, 1981.

[16] Henry Berry Garrett. The charging of spacecraft surfaces. *Reviews of Geophysics*, 19(4):577–616, 1981.

[17] Richard Marchand, Yohei Miyake, Hideyuki Usui, Jan Deca, Giovanni Lapenta, Jean-Charles Matéo-Vélez, RE Ergun, Andrew Sturner, Vincent Génot, Alain Hilgers, et al. Cross-comparison of spacecraft-environment interaction model predictions applied to solar probe plus near perihelion. *Physics of Plasmas (1994-present)*, 21(6):062901, 2014.

[18] VA Davis, MJ Mandell, BM Gardner, IG Mikellides, LF Neergaard, DL Cooke, and J Minor. Validation of NASCAP-2K spacecraft-environment interactions calculations. 2004.

[19] Takanobu Muranaka, Satoshi Hosoda, Jeong-Ho Kim, Shinji Hatta, Koichiro Ikeda, Takamitsu Hamanaga, Mengu Cho, Hideyuki Usui, Hiroko O Ueda, Kiyokazu Koga, et al. Development of multi-utility spacecraft charging analysis tool (MUSCAT). *Plasma Science, IEEE Transactions on*, 36(5):2336–2349, 2008.

[20] Jean-FranÇois Roussel, FranÇois Rogier, Guillaume Dufour, Jean-Charles Mateo-Velez, Julien Forest, Alain Hilgers, David Rodgers, Laurence Girard, and Denis Payan. Spis open-source code: Methods, capabilities, achievements, and prospects. *IEEE Transactions on Plasma Science*, 36(5):2360–2368, 2008.

[21] Stanislas Guillemant. *Study and simulations of spacecraft/plasma interaction phenomena and their effects on low energy plasma measurements*. PhD thesis, Université Paul Sabatier-Toulouse III, 2014.

[22] Yohei Miyake and Hideyuki Usui. New electromagnetic particle simulation code for the analysis of spacecraft-plasma interactions. *Physics of Plasmas (1994-present)*, 16(6):062904, 2009.

[23] Yohei Miyake, Hideyuki Usui, Hirotsugu Kojima, and Hiroshi Nakashima. Plasma particle simulations on stray photoelectron current flows around a spacecraft. *Journal of Geophysical Research: Space Physics*, 117(A9), 2012.

[24] Stefano Markidis, Giovanni Lapenta, et al. Multi-scale simulations of plasma with ipic3d. *Mathematics and Computers in Simulation*, 80(7):1509–1519, 2010.

[25] James G Laframboise. Theory of spherical and cylindrical langmuir probes in a collisionless, Maxwellian plasma at rest. Technical report, DTIC Document, 1966.

[26] Harold M Mott-Smith and Irving Langmuir. The theory of collectors in gaseous discharges. *Physical Review*, 28(4):727, 1926.

[27] Zahida Ehsan, Nodar L Tsintsadze, and S Poedts. A modified orbital motion limited (oml) theory. *arXiv preprint arXiv:1110.6304*, 2011.

[28] SA Self and CH Shih. Theory and measurements for ion collection by a spherical probe in a collisional plasma. *Physics of Fluids (1958-1988)*, 11(7): 1532–1545, 1968.

[29] Kyu-Sun Chung and Ian H Hutchinson. Kinetic theory of ion collection by probing objects in flowing strongly magnetized plasmas. *Physical Review A*, 38(9):4721, 1988.

[30] Francis F Chen. Langmuir probe analysis for high density plasmas. *Physics of Plasmas (1994-present)*, 8(6):3029–3041, 2001.

[31] JE Allen. Probe theory-the orbital motion approach. *Physica Scripta*, 45(5): 497, 1992.

[32] Martin Lampe. Limits of validity for orbital-motion-limited theory for a small floating collector. *Journal of Plasma Physics*, 65(03):171–180, 2001.

[33] Francis F Chen. Langmuir probes in rf plasma: surprising validity of oml theory. *Plasma Sources Science and Technology*, 18(3):035012, 2009.

[34] Boris Delaunay. Sur la sphère vide. *Izv. Akad. Nauk SSSR, Otdelenie Matematicheskii i Estestvennyka Nauk*, 7(793-800):1–2, 1934.

[35] Pascal Jean Frey and Paul-Louis George. *Maillages: applications aux éléments finis*. Hermès Science Publications, 1999.

[36] R Marchand, JY Lu, K Kabin, and R Rankin. Unstructured meshes and finite elements in space plasma modelling: Principles and applications. *Advanced Methods for Space Simulations, edited by H. Usui and Y. Omura, Terrapub, Tokyo*, pages 111–143, 2007.

[37] Anne Poupon. Voronoi and voronoi-related tessellations in studies of protein structure and interaction. *Current opinion in structural biology*, 14(2):233–241, 2004.

[38] Richard Marchand. Ptetra, a tool to simulate low orbit satellite–plasma interaction. *IEEE Transactions on Plasma Science*, 40(2):217–229, 2012.

[39] Eigil Friis-Christensen, H Lühr, and Gauthier Hulot. Swarm: A constellation to study the Earths magnetic field. *Earth, Planets and Space*, 58(4):351–358, 2006.

Appendix

Appendix 1

Geo file of a geometry used to illustrate the effects of multiple reflections

```
    // Gmsh project created on Wed Mar 16 16:29:07 2016
    res=0.1;
zmax=1.8;
zmin=-1.8;
ymax=1.;
ymin=-1.;
xmax=1.4;
xmin=-1.4;
Point(1) = zmin, zmin, zmin, res;
Point(2) = zmax, zmin, zmin, res;
Point(3) = zmin, zmax, zmin, res;
Point(4) = zmax, zmax, zmin, res;
Point(5) = zmin, zmin, zmax, res;
Point(6) = zmax, zmin, zmax, res;
Point(7) = zmin, zmax, zmax, res;
Point(8) = zmax, zmax, zmax, res;
Point(11) = ymin, xmin, xmin, res;
Point(12) = xmin, xmin, xmin, res;
Point(13) = ymin, xmax, xmin, res;
```

```
Point(14) = xmin, xmax, xmin, res;
Point(15) = ymin, xmin, xmax, res;
Point(16) = xmin, xmin, xmax, res;
Point(17) = ymin, xmax, xmax, res;
Point(18) = xmin, xmax, xmax, res;
Point(21) = ymax, xmin, xmin, res;
Point(22) = xmax, xmin, xmin, res;
Point(23) = ymax, xmax, xmin, res;
Point(24) = xmax, xmax, xmin, res;
Point(25) = ymax, xmin, xmax, res;
Point(26) = xmax, xmin, xmax, res;
Point(27) = ymax, xmax, xmax, res;
Point(28) = xmax, xmax, xmax, res;
rad=0.4;
res2=0.2;
zmi=-0.9;
zma=0.9;
Point(31) =  0, 0, zmi, res2;
Point(32) =  rad, 0, zmi, res2;
Point(33) = -rad, 0, zmi, res2;
Point(34) =  0, rad, zmi, res2;
Point(35) =  0, -rad, zmi, res2;
Point(36) =  0., 0., zma, res2;
Point(37) =  rad, 0., zma, res2;
Point(38) = -rad, 0., zma, res2;
Point(39) =  0., rad, zma, res2;
Point(40) = 0., -rad, zma, res2;
Line(1) = 3, 7;
Line(2) = 7, 8;
```

Line(3) = 8, 4;

Line(4) = 4, 3;

Line(5) = 3, 1;

Line(6) = 1, 5;

Line(7) = 7, 5;

Line(8) = 5, 6;

Line(9) = 6, 2;

Line(10) = 2, 1;

Line(11) = 2, 4;

Line(12) = 8, 6;

Line(13) = 18, 17;

Line(14) = 17, 13;

Line(15) = 13, 14;

Line(16) = 14, 18;

Line(17) = 18, 16;

Line(18) = 16, 15;

Line(19) = 15, 11;

Line(20) = 11, 12;

Line(21) = 12, 16;

Line(22) = 14, 12;

Line(23) = 17, 15;

Line(24) = 11, 13;

Line(25) = 28, 27;

Line(26) = 27, 23;

Line(27) = 23, 24;

Line(28) = 24, 28;

Line(29) = 26, 25;

Line(30) = 25, 21;

Line(31) = 21, 22;

Line(32) = 22, 26;

Line(33) = 28, 26;

Line(34) = 24, 22;

Line(35) = 27, 25;

Line(36) = 21, 23;

Circle(37) = 35, 31, 33;

Circle(38) = 33, 31, 34;

Circle(39) = 34, 31, 32;

Circle(40) = 32, 31, 35;

Circle(41) = 40, 36, 38;

Circle(42) = 38, 36, 39;

Circle(43) = 39, 36, 37;

Circle(44) = 37, 36, 40;

Line(45) = 39, 34;

Line(46) = 35, 40;

Line(47) = 38, 33;

Line(48) = 32, 37;

Line Loop(49) = 8, -12, -2, 7;

Plane Surface(50) = 49;

Line Loop(51) = 6, -7, -1, 5;

Plane Surface(52) = 51;

Line Loop(53) = 5, -10, 11, 4;

Plane Surface(54) = 53;

Line Loop(55) = 9, 11, -3, 12;

Plane Surface(56) = 55;

Line Loop(57) = 8, 9, 10, 6;

Plane Surface(58) = 57;

Line Loop(59) = 4, 1, 2, 3;

Plane Surface(60) = 59;

Line Loop(61) = 23, -18, -17, 13;

Plane Surface(62) = 61;

Line Loop(63) = 22, -20, 24, 15;

Plane Surface(64) = 63;

Line Loop(65) = 20, 21, 18, 19;

Plane Surface(66) = 65;

Line Loop(67) = 13, 14, 15, 16;

Plane Surface(68) = 67;

Line Loop(69) = 24, -14, 23, 19;

Plane Surface(70) = 69;

Line Loop(71) = 17, -21, -22, 16;

Plane Surface(72) = 71;

Line Loop(73) = 29, -35, -25, 33;

Plane Surface(74) = 73;

Line Loop(75) = 36, 27, 34, -31;

Plane Surface(76) = 75;

Line Loop(77) = 31, 32, 29, 30;

Plane Surface(78) = 77;

Line Loop(79) = 25, 26, 27, 28;

Plane Surface(80) = 79;

Line Loop(81) = 32, -33, -28, 34;

Plane Surface(82) = 81;

Line Loop(83) = 30, 36, -26, 35;

Plane Surface(84) = 83;

Line Loop(85) = 44, 41, 42, 43;

Plane Surface(86) = 85;

Line Loop(87) = 40, 37, 38, 39;

Plane Surface(88) = 87;

Line Loop(89) = 47, 38, -45, -42;

Ruled Surface(90) = 89;

Line Loop(91) = 46, 41, 47, -37;

Ruled Surface(92) = 91;

Line Loop(93) = 46, -44, -48, 40;

Ruled Surface(94) = 93;

Line Loop(95) = 39, 48, -43, 45;

Ruled Surface(96) = 95;

Surface Loop(97) = 52, 58, 50, 56, 54, 60;

Surface Loop(98) = 66, 64, 72, 62, 70, 68;

Surface Loop(99) = 90, 92, 94, 86, 96, 88;

Surface Loop(100) = 84, 78, 76, 80, 74, 82;

Volume(101) = 97, 98, 99, 100;

Physical Surface(102) = 60, 50, 58, 52, 54, 56;

Physical Surface(103) = 64, 66, 68, 62, 72, 70;

Physical Surface(104) = 92, 88, 94, 86, 90, 96;

Physical Surface(105) = 78, 76, 80, 74, 82, 84;

Physical Volume(106) = 101;